Model-independent measurement of the matter-radiation equality scale in DESI 2024

B. Bahr-Kalus, ^{1,2,3,4,*} D. Parkinson, ^{4,5,†} K. Lodha, ^{4,5} E. Mueller, ⁶ E. Chaussidon, ⁷ A. de Mattia, ⁸ D. Forero-Sánchez, ⁹ J. Aguilar, ⁷ S. Ahlen, ¹⁰ D. Bianchi, ^{11,12} D. Brooks, ¹³ T. Claybaugh, ⁷ A. Cuceu, ⁷ A. de la Macorra, ¹⁴ P. Doel, ¹³ A. Font-Ribera, ¹⁵ E. Gaztañaga, ^{16,17,18} S. Gontcho A. Gontcho, ⁷ G. Gutierrez, ¹⁹ K. Honscheid, ^{20,21,22} D. Huterer, ^{23,24} M. Ishak, ²⁵ R. Kehoe, ²⁶ S. Kent, ^{19,27} D. Kirkby, ²⁸ T. Kisner, ⁷ A. Kremin, ⁷ O. Lahav, ¹³ M. Landriau, ⁷ L. Le Guillou, ²⁹ C. Magneville, ⁸ M. Manera, ^{15,30} P. Martini, ^{20,22,31} A. Meisner, ³² R. Miquel, ^{15,33} J. Moustakas, ³⁴ S. Nadathur, ¹⁷ N. Palanque-Delabrouille, ^{8,7} W. J. Percival, ^{35,36,37} F. Prada, ³⁸ I. Pérez-Ràfols, ³⁹ A. J. Ross, ^{20,31,22} G. Rossi, ⁴⁰ L. Samushia, ^{41,42,43} E. Sanchez, ⁴⁴ D. Schlegel, ⁷ M. Schubnell, ^{23,24} H. Seo, ⁴⁵ J. Silber, ⁷ D. Sprayberry, ³² G. Tarlé, ²⁴ B. A. Weaver, ³² R. Zhou, ⁷ and H. Zou, ⁴⁶

(DESI Collaboration) ¹INAF, Osservatorio Astrofisico di Torino, Via Osservatorio 20, 10025 Pino Torinese, Italy ²Dipartimento di Fisica, Università degli Studi di Torino, Via Pietro Giuria 1, 10125 Torino, Italy ³INFN, Sezione di Torino, Via Pietro Giuria 1, 10125 Torino, Italy ⁴Korea Astronomy and Space Science Institute, 776, Daedeokdae-ro, Yuseong-gu, Daejeon 34055, Republic of Korea ⁵University of Science and Technology, 217 Gajeong-ro, Yuseong-gu, Daejeon 34113, Republic of Korea ⁶Department of Physics and Astronomy, University of Sussex, Brighton BN1 90H, United Kingdom Lawrence Berkeley National Laboratory, 1 Cyclotron Road, Berkeley, California 94720, USA ⁸IRFU, CEA, Université Paris-Saclay, F-91191 Gif-sur-Yvette, France ⁹Institute of Physics, Laboratory of Astrophysics, École Polytechnique Fédérale de Lausanne (EPFL), Observatoire de Sauverny, Chemin Pegasi 51, CH-1290 Versoix, Switzerland ¹⁰Department of Physics, Boston University, 590 Commonwealth Avenue, Boston, Massachusetts 02215 USA ¹Dipartimento di Fisica "Aldo Pontremoli," Università degli Studi di Milano, Via Celoria 16, I-20133 Milano, Italy ¹²INAF-Osservatorio Astronomico di Brera, Via Brera 28, 20122 Milano, Italy ¹³Department of Physics and Astronomy, University College London, Gower Street, London, WC1E 6BT, United Kingdom ¹⁴Instituto de Física, Universidad Nacional Autónoma de México, Circuito de la Investigación Científica, Ciudad Universitaria, Ciudad de México Código Postal 04510, México ¹⁵Institut de Física d'Altes Energies (IFAE), The Barcelona Institute of Science and Technology, Edifici Cn, Campus UAB, 08193, Bellaterra (Barcelona), Spain ¹⁶Institut d'Estudis Espacials de Catalunya (IEEC), c/Esteve Terradas 1, Edifici RDIT, Campus PMT-UPC, 08860 Castelldefels, Spain ¹⁷Institute of Cosmology and Gravitation, University of Portsmouth, Dennis Sciama Building, Portsmouth, PO1 3FX, United Kingdom ¹⁸Institute of Space Sciences, ICE-CSIC, Campus UAB, Carrer de Can Magrans s/n, 08913 Bellaterra, Barcelona, Spain ¹⁹Fermi National Accelerator Laboratory, PO Box 500, Batavia, Illinois 60510, USA ²⁰Center for Cosmology and AstroParticle Physics, The Ohio State University, 191 West Woodruff Avenue, Columbus, Ohio 43210, USA ²¹Department of Physics, The Ohio State University, 191 West Woodruff Avenue, Columbus, Ohio 43210, USA ²²The Ohio State University, Columbus, 43210 Ohio, USA ²³Department of Physics, University of Michigan, 450 Church Street, Ann Arbor, Michigan 48109, USA ²⁴University of Michigan, 500 South State Street, Ann Arbor, Michigan 48109, USA ⁵Department of Physics, The University of Texas at Dallas, 800 West Campbell Road, Richardson, Texas 75080, USA ²⁶Department of Physics, Southern Methodist University, 3215 Daniel Avenue, Dallas, Texas 75275, USA ²⁷Department of Astronomy and Astrophysics, University of Chicago, 5640 South Ellis Avenue, Chicago, Illinois 60637, USA ²⁸Department of Physics and Astronomy, University of California, Irvine, California 92697, USA ²⁹Sorbonne Université, CNRS/IN2P3, Laboratoire de Physique Nucléaire et de Hautes Energies (LPNHE), FR-75005 Paris, France

```
<sup>30</sup>Departament de Física, Serra Húnter, Universitat Autònoma de Barcelona, 08193 Bellaterra
                                                 (Barcelona), Spain
             <sup>31</sup>Department of Astronomy, The Ohio State University, 4055 McPherson Laboratory,
                                140 W 18th Avenue, Columbus, Ohio 43210, USA
    <sup>32</sup>United States National Science Foundation National Optical-Infrared Astronomy Research Laboratory,
                             950 North Cherry Avenue, Tucson, Arizona 85719, USA
<sup>33</sup>Institució Catalana de Recerca i Estudis Avançats, Passeig de Lluís Companys, 23, 08010 Barcelona, Spain
<sup>34</sup>Department of Physics and Astronomy, Siena College, 515 Loudon Road, Loudonville, New York 12211, USA
                        <sup>35</sup>Department of Physics and Astronomy, University of Waterloo,
                       200 University Avenue West, Waterloo, Ontario N2L 3G1, Canada
 <sup>36</sup>Perimeter Institute for Theoretical Physics, 31 Caroline Street North, Waterloo, Ontario N2L 2Y5, Canada
                           <sup>37</sup>Waterloo Centre for Astrophysics, University of Waterloo,
                       200 University Avenue West, Waterloo, Ontario N2L 3G1, Canada
    <sup>38</sup>Instituto de Astrofísica de Andalucía (CSIC), Glorieta de la Astronomía, s/n, E-18008 Granada, Spain
                     <sup>39</sup>Departament de Física, EEBE, Universitat Politècnica de Catalunya,
                                 c/Eduard Maristany 10, 08930 Barcelona, Spain
                           <sup>40</sup>Department of Physics and Astronomy, Sejong University,
                       209 Neungdong-ro, Gwangjin-gu, Seoul 05006, Republic of Korea
                       <sup>41</sup>Abastumani Astrophysical Observatory, Tbilisi, GE-0179, Georgia
    <sup>42</sup>Department of Physics, Kansas State University, 116 Cardwell Hall, Manhattan, Kansas 66506, USA
            <sup>43</sup>Faculty of Natural Sciences and Medicine, Ilia State University, 0194 Tbilisi, Georgia
                          <sup>44</sup>CIEMAT, Avenida Complutense 40, E-28040 Madrid, Spain
 <sup>45</sup>Department of Physics and Astronomy, Ohio University, 139 University Terrace, Athens, Ohio 45701, USA
       <sup>b</sup>National Astronomical Observatories, Chinese Academy of Sciences, A20 Datun Road, Chaoyang
                              District, Beijing, 100101, People's Republic of China
```

(Received 28 May 2025; accepted 29 August 2025; published 24 September 2025)

The peak of the matter power spectrum, known as the turnover (TO) scale, is determined by the horizon size at the time of matter-radiation equality. This scale can serve as a standard ruler, independent of other features in the matter power spectrum, such as baryon acoustic oscillations (BAO). Here, we present the first detection of the turnover in the galaxy autopower spectrum, utilizing the distribution of quasars and luminous red galaxies (LRG) measured by the Dark Energy Spectroscopic Instrument (DESI) during its first year of survey operations in a model-independent manner. To avoid confirmation bias, we first analyze the data using data blinding methods designed for the DESI baryon acoustic oscillation, redshift space distortion and scale-dependent bias signals. We measure the angle-averaged dilation distance $D_{\rm V}(z=$ 1.651) = $(38.1 \pm 2.5)r_{\rm H}$ from the quasars and $D_{\rm V}(z=0.733)=(21.8 \pm 1.0)r_{\rm H}$ from the LRG sample in units of the horizon $r_{\rm H}$ at the matter-radiation-equality epoch. Combining these two constraints and assuming a flat Λ CDM model with three standard neutrino species, we can translate this into a constraint of $\Omega_{\rm m}h^2=0.139^{+0.036}_{-0.046}$. We can break the $\Omega_{\rm m}$ - H_0 degeneracy with low-redshift distance measurements from type-Ia supernova (SN) data from Pantheon+, we obtain a sound-horizon free estimate of the Hubble-Lemaître parameter of $H_0 = 65.2^{+4.9}_{-6.2}$ km/s/Mpc, consistent with sound-horizon dependent DESI measurements. On the other hand, combining the DESI BAO and TO, we find a truly DESI-only measurement of $H_0 = 74.0^{+3.5}_{-3.5}$ km/s/Mpc, in line with DESI-only full-shape results where the soundhorizon scale is marginalized out. This discrepancy in H_0 can be reconciled in a w_0w_a CDM cosmology, where the combination of DESI BAO and TO data yields $H_0 = 66.5 \pm 7.2$ km/s/Mpc.

DOI: 10.1103/yqm1-ybbv

I. INTRODUCTION

The distribution of matter in the Universe is observed through the distribution of tracer particles, such as galaxies, quasistellar objects (QSOs) or Lyman-alpha absorption

*Contact author: benedict.bahrkalus@inaf.it †Contact author: davidparkinson@kasi.re.kr systems at low-redshift or hot and cold spots in the cosmic microwave background (CMB) at high-redshift. The formation of structures during two epochs is linked through gravitational collapse, as the seeds of structure formation are fixed during the relativistic era. Matter perturbations have only just begun to grow when the CMB photons are emitted during recombination and the size of fluctuations $\frac{\delta \rho}{\rho} \sim 10^{-5}$. This early era of linear growth, where cold dark

matter (CDM) perturbations can grow without the restoring force of photon pressure while the baryon perturbations experience acoustic oscillations, starts at the epoch of matter-radiation equality. At this epoch the two fluids have equal energy density, and so any (small-scale) perturbation that entered the horizon before this epoch is retarded in its growth, whereas the larger perturbations that enter after experience continual enhancement. As such, the horizon scale at matter-radiation equality appears in the matter density power spectrum as a peak.

This matter-radiation equality scale (also known as the power spectrum turnover) is fixed in comoving coordinates, similar to the baryon acoustic oscillation (BAO) sound horizon, and can be measured in the same way at low redshift, using galaxy redshift surveys. Since the scale can be measured in a (relatively) cosmologically independent way, it can be used as a standard ruler to probe the expansion history of the Universe. The scale is calibrated by the ratio of the relativistic vs nonrelativistic energy densities, where the total energy density of the relativistic material in the Universe includes the sum of the photon and neutrino energy densities.

Making an accurate detection of the equality scale from the matter power spectrum requires a much larger volume than is needed for the BAO. A first indication was attempted using data from the WiggleZ Dark Energy Survey [1], with an effective survey volume of only $0.84~(\mathrm{Gpc/}h)^3$. A more solid measurement of a power spectrum inflexion point was achieved using the eBOSS quasar sample [2], however, there was no clear evidence for a positive large-scale slope of the power spectrum. The power spectrum turnover has recently been detected in the projected clustering of quasars in the Gaia-unWISE quasar catalog, Quaia, and its cross-correlation with CMB lensing data from Planck [3].

In this work, we aim to improve on our eBOSS power spectrum turnover measurement with a QSO sample with a three times larger effective volume and an additional tracer from the Dark Energy Spectroscopic Instrument (DESI), a multiobject fiber-fed spectroscopic system with 5000 fibers covering the focal plane with a \sim 3° field of view [4–7]. The spectrograph is mounted on the focal plane of the Mayall Telescope at Kitt Peak National Observatory, Arizona [8]. The DESI spectrograph is being used for the large-scale structure galaxy redshift survey that started in 2020, which will measure the spectra of 35 million galaxies over 5 years [9].

The goal of the DESI is to determine the nature of dark energy through the most precise measurement of the expansion history of the universe ever obtained [10]. DESI was designed to meet the definition of a stage IV dark energy survey with only a 5-year observing campaign. Forecasts for DESI [9] predict a factor of approximately five to ten improvement on the size of the error ellipse of the dark energy equation of state parameters w_0 and w_a relative to previous stage-III experiments. Here, the constraints on the dark energy parameters are primarily coming from

measurements of the BAO standard ruler, which is sensitive to both the angular diameter distance and the Hubble parameter, evaluated at the redshift of the galaxy sample.

The matter-radiation equality scale and the BAO scale differ in the physical mechanisms that generate them, and so are calibrated differently. Recent analyses of DESI BAO [11,12] have either marginalized over this physical sound horizon scale (to use the BAO as relative-size rulers) or else combined the BAO data at low-redshift with measurements of the CMB temperature and polarization anisotropies at high redshift, which provide very accurate predictions of the sound horizon at the drag epoch [13]. The matterradiation equality scale can be calibrated without reference to the CMB power spectrum, requiring only a knowledge of the total relativistic energy density of the Universe, which comes from the monopole CMB temperature, plus our understanding of the neutrino sector. Because of this, it can be used to make a measurement of the physical matter density $(\Omega_m h^2)$, in contrast to the BAO that are sensitive to the matter density as a fraction of the critical density, Ω_m . Further, our analysis method extracts the matter-radiation equality scale in a model-independent fashion, and (as we will show) our measurements have very small covariance with the DESI BAO measurements.

This work is one of a number of complementary DESI projects that use sound-horizon-independent methods to obtain a measurement of H_0 . Our companion projects achieve this by either marginalizing over the sound horizon [14], by using only energy densities [15], or by using other power spectrum or correlation function features that depend on the epoch of matter-radiation equality [16–18].

In Sec. II we describe the physics of the matter-radiation scale, and in Sec. III we describe the methodology used to measure it. In Sec. IV we describe the DESI data, as well as the mock catalogs that we used to validate our method and compute the covariances. In Sec. V we give the measured values and errors of the matter-radiation scale, and the inferred cosmological parameter constraints. We summarize our findings in Sec. VI.

II. THE HORIZON SCALE AT MATTER-RADIATION EQUALITY

The epoch of matter-radiation equality is a major changing point in the history of the Universe due to the change in dynamics, in the growth rate and propagation of the density perturbations. As the expansion decelerates, the Hubble-Lemaître rate falls, and primordial perturbations at super-horizon scales can reenter the horizon, restarting their evolution. However, for those perturbations that already reenter during radiation domination, the pressure of the relativistic mass-energy prevents gravitational collapse. It is only when nonrelativistic matter starts to dominate the dynamics that density perturbations can grow. The specific horizon size at the epoch of matter-radiation equality is a significant scale in the structure formation history of the

Universe, depending only on its history up until then, and unaffected by any future change in the dynamics (e.g., curvature, dark energy). It is given by

$$r_{\rm H} = c \int_0^{a_{\rm eq}} \frac{\mathrm{d}a}{a^2 H(a)},\tag{1}$$

where the scale factor at matter-radiation equality $a_{\rm eq} = (1+z_{\rm eq})^{-1} = \Omega_{\rm r}/\Omega_{\rm m}$ can be expressed in terms of the ratio of the radiation and matter density parameters. This simple equation, used in [2], becomes slightly more complicated in the presence of massive neutrinos.

For massless neutrinos, the energy density scales as a^{-4} in the same manner as photons. However, massive neutrinos are relativistic in the early Universe but become nonrelativistic later, functioning as a form of warm dark matter that slows gravitational collapse. Most cosmological Boltzmann codes treat the massive neutrinos in this manner, as a fluid with some nonconstant equation of state. The evolution of the different density values is shown in Fig. 1.

Since massive neutrinos become nonrelativistic at late time, they should be considered as part of the relativistic energy density budget when computing the redshift of matter radiation equality. In practice, this means that when computing this equality redshift, the massive neutrino (or neutrinos) should be treated as though it were massless, and

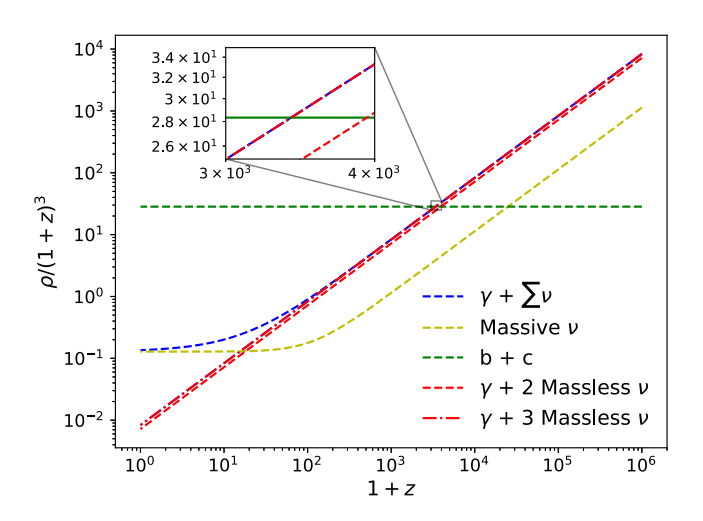


FIG. 1. The evolution of the mass density of different components as a function of redshift, assuming a single massive neutrino species with mass 0.06 eV (golden line), and two other massless species (combined with the photons in the red dashed line). The equality redshift $z_{\rm eq}$ is given by the point where the blue (total relativistic energy density) and green (total nonrelativistic energy density) lines coincide. For comparison, we also show the combined neutrino energy density in a cosmology where all neutrinos are massless as a red dot-dashed line. We can observe, that at the matter-radiation-equality epoch, the massive neutrino effectively behaves like a massless neutrino.

the total effective number of neutrino species $N_{\rm eff}$ adjusted accordingly. So, the redshift of equality is given by

$$a_{\rm eq} = (1 + z_{\rm eq})^{-1} = \frac{\rho_{\gamma} + \rho_{\nu}}{\rho_{\rm b} + \rho_{\rm cdm}},$$
 (2)

where the neutrino density is computed assuming all species are massless,

$$\rho_{\nu} = N_{\text{eff}} \frac{7\pi^2}{120} T_{\nu}^4. \tag{3}$$

Here the neutrino temperature is

$$T_{\nu} = \left(\frac{11}{4}\right)^{-1/3} T_{\gamma},\tag{4}$$

and the effective number of neutrino species $N_{\rm eff}$ is equal to the total effective number of neutrino species, including massive and massless.

Considering the early Universe (i.e., $a < a_{\rm eq}$) being composed only of photons, effectively relativistic neutrinos, baryonic, and cold dark matter, we can evaluate the integral of (1) to express the horizon scale as

$$r_{\rm H} = \frac{2c(\sqrt{2} - 1)\sqrt{a_{\rm eq}}}{H_0\sqrt{\Omega_{\rm bc}}} \tag{5}$$

which is inversely proportional to the square root of $\omega_{\rm bc} = \omega_{\rm b} + \omega_{\rm cdm}$, where $\omega_i = \Omega_i h^2$ denotes the physical energy density of fluid i, and be denotes baryonic and cold dark matter, explicitly excluding massive neutrinos.

Following [19], we can define the equality wave number as $k_{\rm eq} = a_{\rm eq} H(a_{\rm eq})$. Under the same assumptions that led to (5), it is straightforward to relate this quantity to $r_{\rm H}$ as [17]

$$k_{\rm eq} = 2(2 - \sqrt{2})r_{\rm H}^{-1} \tag{6}$$

This $k_{\rm eq}$ is approximately but not exactly the turnover scale $k_{\rm TO}$. $k_{\rm TO}$ has a weak dependence on the baryon density $\omega_{\rm b}$. The two scales can be related by the fitting formula [17] $k_{\rm TO} = \frac{0.194}{\omega_{\rm b}^{0.321}} (k_{\rm eq} \, {\rm Mpc} \, h^{-1})^{0.685-0.121 \, {\rm log}_{10}(\omega_{\rm b})}$ to connect the two scales. However, here we are going to take a more accurate approach and find the maximum of fiducial power spectra computed using the COSMOPRIMO interface to the CLASS Boltzmann solver [20].

III. METHODS

A. Fiducial cosmology

Like the BAO analyses [11,12], our analysis here uses a fiducial cosmology to convert redshifts into distances.

https://github.com/cosmodesi/cosmoprimo.

Thus, our distance measurements are relative to this fiducial cosmology. Our fiducial cosmology matches the average cosmological parameter values from the Planck 2018- Λ CDM base_plikHM_TTTEEE_lowl_lowE_lensing chains [21]. The key parameters are $\omega_{\rm b}=0.02237, \omega_{\rm cdm}=0.1200,$ $h=0.6736,\;$ the effective number of ultrarelativistic species $N_{\rm ur}=2.0328$ and one massive neutrino with $\omega_{\nu}=0.00064420.$ This is the fiducial cosmology throughout DESI and also corresponds to the cosmology used when simulating the 25 base AbacusSummit boxes. Computing the power spectrum for this fiducial cosmology using COSMOPRIMO, we find a peak at

$$k_{\text{TO,fid}} = 16.5 h/\text{Gpc}.$$
 (7)

In analogy to the BAO analyses, we define a dilation parameter

$$\alpha_{\rm TO} = \frac{k_{\rm TO}}{k_{\rm TO fid}}.$$
 (8)

Even though the turnover scale $k_{\rm TO}$ only approximates the equality scale $k_{\rm eq}$ (cf. Sec. II), mock analyses show that

$$\alpha_{\rm TO} = \frac{D_{\rm V}(z)}{D_{\rm V,fid}(z)} \frac{r_{\rm H,fid}}{r_{\rm H}} \tag{9}$$

in analogy to the isotropic BAO (where $D_{\rm V}(z)=\sqrt[3]{\frac{cz}{H(z)}D_{\rm M}^2(z)}$ and $D_{\rm M}(z)$ is the comoving distance to redshift z) works well to link $k_{\rm TO}$ to cosmology, as long as the fiducial cosmology is not unreasonably different from the true cosmology. We show in Appendix A and Fig. 12 that Eq. (9) works well for a wide range of parameter values. Whereas the modeling used for our eBOSS analysis [2] based on a fitting formula to link $k_{\rm eq}$ and $k_{\rm TO}$ yields biased results in cases where the true cosmology has either a high value of h or a low value of $\omega_{\rm cdm}$.

In order to compute the fiducial horizon size $r_{\rm H,fid}$, we use (2)–(4) to first compute the redshift

$$z_{\text{eq,fid}} = 3408 \tag{10}$$

at which matter-radiation equality happened, which corresponds to a scale factor $a_{\rm eq}=2.93\times 10^{-4}$ and, in turn, to

$$r_{\text{H.fid}} = 112.7 \text{ Mpc.}$$
 (11)

B. Parametrization

Close to the turnover, we model the galaxy power spectrum monopole as $\hat{P}(k) = K(b_1)P_{\text{template}}(k) + s_{n,0}$ where P_{template} is parametrized in the following model-independent way:

$$P_{\text{template}}(k) = \begin{cases} P_{\text{TO,fid}}^{1-mx^2} & \text{for } \frac{k}{k_{\text{TO,fid}}} < \alpha_{\text{TO}} \\ P_{\text{TO,fid}}^{1-nx^2} & \text{for } \frac{k}{k_{\text{TO,fid}}} \ge \alpha_{\text{TO}}, \end{cases}$$
(12)

with $P_{\mathrm{TO,fid}}=P_{\mathrm{fid}}(k_{\mathrm{TO,fid}}),$ $x=\frac{\ln(k\,\mathrm{Mpc}/h)}{\ln(lpha_{\mathrm{TO}}k_{\mathrm{TO,fid}}\,\mathrm{Mpc}/h)}-1$ and the Kaiser factor $K(b_1)=b_1^2+\frac{2}{3}b_1f_{\rm fid}+\frac{1}{5}f_{\rm fid}^2$ [22] evaluated for the growth rate $f_{\rm fid}$ for the fiducial cosmology. We vary in total five parameters in our fits: the scaling parameter α_{TO} , the slope parameters m and n, the linear bias parameter b_1 , and the residual shot noise $s_{n,0}$. This parametrization is equivalent to the one used in measurements of the matter-radiation equality scale using the WiggleZ Dark Energy Survey [1] and the extended Baryon Oscillation Spectroscopic Survey (eBOSS) quasar sample [2,23]. While [1,2,23] also employ two slope parameters m and n, here, we express the position of the turnover by a scaling parameter α_{TO} and the power spectrum amplitude by the linear bias parameter b_1 . In this way, we are closer to the BAO implementation in DESILIKE² and, at the same time, emphasize that (12) is defined with respect to a fiducial template power spectrum $P_{\rm fid}(k)$ which sets the power spectrum peak position $k_{\rm TO,fid}$ and its amplitude $P_{\rm TO,fid}$.

Of course, the parametrization given in (12) breaks down the further we are from the turnover scale due to the BAO, nonlinear clustering and other small-scale effects. We could prevent these from biasing our results by either an aggressive scale cut or modeling these effects; however, in the former case, we lose valuable broad-band information, and in the latter, we lose model independence. Therefore, we follow [2,23] and deproject out the modeling systematic as follows:

- (1) We compute the mean of the power spectra of 1000 EZmock realizations $\bar{P}_{\text{mock}}(k)$ (cf. Sec. IVA). Note that this step differs slightly from the eBOSS analysis [2,23], where the fiducial power spectrum computed by CAMB was used instead. This change ensures that the window function, fiber assignment effects, etc. are properly included (cf. Sec. IVA).
- (2) We fit (12) to the mean mock power spectrum over the same k-range as the data, fixing $\alpha_{TO} = 1$ and imposing weights inverse to $\sigma^2(k) = (k k_{TO,fid})^2$. While this acts like a variance, this is not any data-informed quantity but rather a choice. The goal of this choice is to estimate the modeling error, and as (12) parametrizes the power spectrum well close to the turnover scale, we chose σ to reflect the distance between k and the expected turnover scale. We call the best-fitting power spectrum $P_{bf}(k)$.
- (3) The *k*-dependence of our modeling inaccuracy can then be described by $f(k) = \bar{P}_{\text{mock}}(k) P_{\text{bf}}(k)$. We free the amplitude of our modeling systematic by

²https://github.com/cosmodesi/desilike.

introducing a nuisance parameter τ . The true power spectrum then reads $P_{\text{true}}(k) = \hat{P}(k) + \tau f(k)$. Assuming independence between $\hat{P}(k)$ and f(k), the covariance taking our modeling inaccuracy into account is given by $\hat{C}(k_1,k_2) = C_{\text{true}}(k_1,k_2) + \tau^2 f(k_1) f(k_2)$. We can analytically marginalize out the nuisance parameter τ by taking its limit to infinity when inverting $\hat{C}(k_1,k_2)$, yielding

$$\hat{C}^{-1}(k,q) = C_{\text{true}}^{-1}(k,q) - \Delta C(k,q),$$
 (13)

with

$$\Delta C(k,q) = \frac{\sum_{\mathcal{A}, \vec{\pi}} C_{\text{true}}^{-1}(k, \mathcal{A}) f(\mathcal{A}) f(\vec{\pi}) C_{\text{true}}^{-1}(\vec{\pi}, q)}{\sum_{\mathcal{A}, \vec{\pi}} f(\mathcal{A}) C_{\text{true}}^{-1}(\mathcal{A}, \vec{\pi}) f(\vec{\pi})}.$$
(14)

C. Likelihood and fitting

In our eBOSS analysis [2], we identified a discrepancy in determining k_{TO} when adhering to the conventional assumption of a Gaussian likelihood for the power spectrum. To rectify this bias, we opted for an alternative approach by employing a likelihood derived from a Box-Cox transformation [24] applied to the gamma distribution approximating the hypo-exponential distribution of a binned, window-convolved power spectrum of a Gaussian random field [25]. It is important to note that in this approximation, the number of available k-modes corresponds to the diagonal elements of the precision matrix $\hat{C}^{-1}(k,k)$. However, the application of (14) diminishes the presumed count of modes, which inadvertently incorrectly enhances the non-Gaussian characteristics of the likelihood at smaller scales. Consequently, we have decided not to use the likelihood model employed in the eBOSS TO analysis and utilize instead a conventional Gaussian likelihood defined as:

$$\chi^2 = \sum_{(k_1, k_2) = k_{\min}}^{k_{\max}} \Delta P(k_1) \hat{C}^{-1}(k_1, k_2) \Delta P(k_2), \quad (15)$$

where $\Delta P(k) = \tilde{P}(k) - P_{\rm conv}(k)$. We will demonstrate in Sec. IV A that for DESI, this approach provides an unbiased measurement of the turnover scale.

We choose of $k_{\rm min}=0.004~h/{\rm Mpc}$ and $k_{\rm max}=0.2~h/{\rm Mpc}$ to be the same values as in the eBOSS turnover analysis [2]. Our choice of $k_{\rm min}$ is slightly more conservative than in the DESI primordial non-Gaussianity (PNG) analysis [26] which uses the same data. Larger scales are impacted by geometrical effects and, more importantly, imperfect correction of imaging systematics. On the other hand, our $k_{\rm max}$ is significantly larger than $k_{\rm max}=0.08~h/{\rm Mpc}$ chosen for the PNG measurement [26]. We can use this larger value

because our method down-weights these small scales, effectively using only the broadband information from the power spectrum.

We show in Fig. 2 the posterior contours of turnover parameters obtained from minimizing (15) for the mean power spectrum of DESI Y1 LRG and QSO EZmock realistations (cf. Sec. IVA), assuming the PNG analysis $k_{\text{max}} = 0.08 \ h/\text{Mpc}$, the eBOSS turnover analysis $k_{\text{max}} =$ 0.2 h/Mpc, and an intermediate $k_{\text{max}} = 0.15 \text{ h/Mpc}$. As expected, we see significant differences in the marginalized 1D posterior of the small-scale slope parameter *n*. However, the quantities we care about—the fraction of the posterior volume with m > 0 and the value of α_{TO} —remain remarkably stable. The probability of not detecting the turnover feature [i.e., $\mathcal{P}(m \leq 0)$] is remarkably stable when changing k_{max} , diminishing from 21.6% in mock LRGs at $k_{\text{max}} =$ $0.08\ h/\mathrm{Mpc}$ to 21.1% at higher k_{max} , and changing from 0.06% at $k_{\text{max}} = 0.08 \ h/\text{Mpc}$, to 0.04% at $k_{\text{max}} =$ $0.15 \ h/\mathrm{Mpc}$ and 0.08% at $k_{\mathrm{max}} = 0.2 \ h/\mathrm{Mpc}$ with mock QSOs. The maximum a posteriori value of α_{TO} is also stable under variations of k_{max} (LRG: 0.99, 1.002, 0.995; QSO: 1.01, 1.007, 1.004, for $k_{\text{max}} = [0.08, 0.15, 0.2]h/\text{Mpc}$, respectively). What we do notice for α_{TO} is that by carving away posterior space using small-scale broadband information on n, we reduce the standard deviation on α_{TO} from 0.22 to 0.091 and 0.071 with the mock LRGs and from 0.11 to 0.085 and 0.080 with the mock QSOs, again for $k_{\text{max}} = [0.08, 0.15, 0.2] h/\text{Mpc}$. Therefore, we have chosen

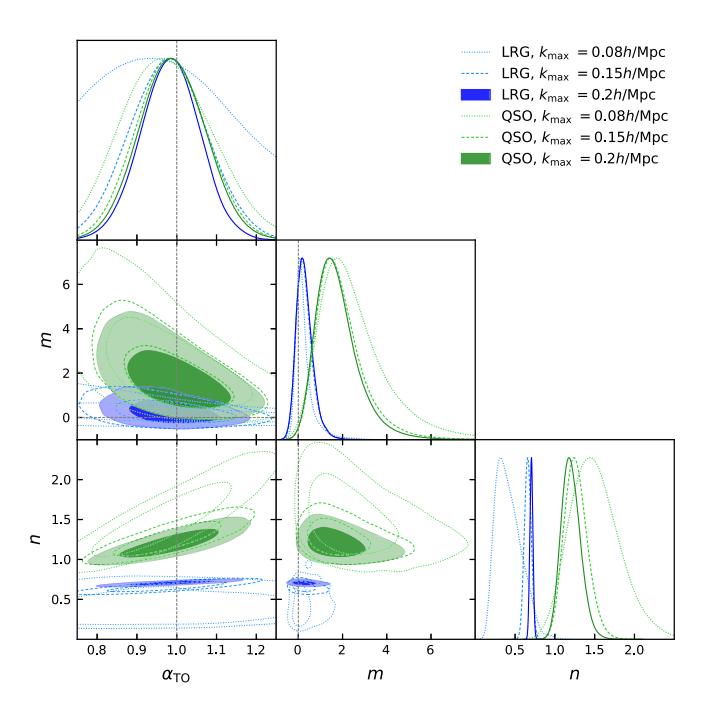


FIG. 2. Constraints on turnover parameters from the mean of DESI Y1 LRG and QSO EZmock power spectra obtained with different values of $k_{\rm max}$. The filled contours correspond to the fiducial $k_{\rm max}=0.2~h/{\rm Mpc}$ used throughout this article.

 $k_{\text{max}} = 0.2 \ h/\text{Mpc}$ for our analysis, as it provides tighter yet stable constraints on the parameters of interest.

All inferences are performed using the EMCEE sampler³ [27] within the DESILIKE framework. A practical outline of our analysis pipeline is available as a Jupyter notebook on the COSMODESI GitHub page.⁴

IV. DATA

We make use of data from the first year of spectroscopic observations carried out with the DESI instrument [4] mounted on the Nicholas U. Mayall Telescope at Kitt Peak National Observatory on Iolkam Du'ag in Arizona from the 14th of May, 2021, until the 14th of June, 2022. Each observation field is covered by a "tile," consisting in a set of targets [28] selected from the photometric catalogs of the 9th public data release of the DESI Legacy Imaging Surveys [29]⁵ and assigned to each of the 5000 fibers in the telescope's focal plane. The observed data are processed by the DESI spectroscopic pipeline [30]. The covered tile surface area is about 7,500 deg², i.e., roughly half of DESI's expected final coverage of 14,200 deg². The extragalactic targets are defined to fall into the four following classes: the bright galaxy sample (BGS, [31]), luminous red galaxies (LRG, [32]), emission line galaxies (ELG [33]), and quasars (QSO [34]). As we need as much volume as possible to observe the large-scale feature of the power spectrum turnover, we do not consider the BGS sample, extending only to a maximum redshift of $z_{\text{max}} = 0.6$, for this analysis. Although the ELG sample covers the redshift range of 1.1 < z < 1.6 (overlapping with both LRGs and QSOs), significant efforts to control systematic effects at scales much larger than the BAO have not yet been fully successful [35]. Hence, we only use the LRG and OSO samples for this study, which we describe in the following subsections. For a more general and technical overview of the catalog building, we refer to [36].

In particular, we use the power spectra and covariance matrices (cf. Fig. 3) generated for constraints on the scale-dependent bias signature of local-type PNG [26]. We will briefly summarize how they are obtained but refer the reader to the primordial non-Gaussianity paper for a detailed description of how they have been obtained. Unlike the DESI key analyses [11–13,37], we make use of the full available redshift ranges of the LRG and QSO samples, i.e., we do not subdivide the LRG sample into redshift bins, and we include QSOs at redshifts higher than z=2.1 which are principally targeted for Ly- α forest analyses.

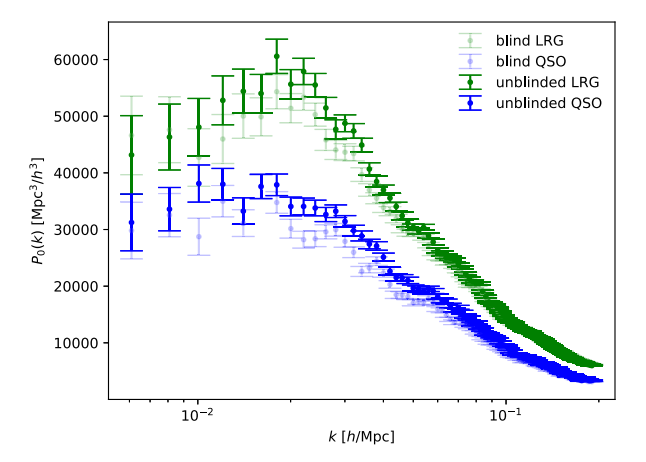


FIG. 3. DESI Y1 LRG and QSO power spectra. Pale data points and error bars show the blinded data, whereas opaque ones the data after unblinding. The solid curves represent the best fit (cf. Sec. V). The apparent mismatch between data and best fit at small scales are the effect of the mode deprojection of the modeling uncertainty at these scales far from the power spectrum peak [cf. Eq. (14)].

The QSO sample [34] used here thus contains 1,189,129 objects (thus about 40% larger than the standard QSO clustering sample with 856,652 objects and more than three times as large as the eBOSS QSO sample [38] with 343,708 objects used in [2,23]) with redshift values ranging from 0.8 to 3.1. The effective redshift is $z_{\rm eff} = 1.651$ [26] when using Feldman-Kaiser-Peacock (FKP) weights [39]. Note that this is lower than when using the optimal redshift weights applied in the DESI PNG analysis [26].

Apart from containing more objects than the eBOSS QSO sample, the DESI QSO sample covers a larger area, as well as a higher density due to the high priority given to QSOs in the fiber assignment process. This results in an effective volume at the turnover scale about three times larger than that of the eBOSS QSO sample.

The LRG sample used here combines all three LRG subsamples used in the DESI key analyses [11–13,37]. Its effective redshift amounts to $z_{\rm eff} = 0.733$ using standard FKP weights [26].

Variations in completeness, imaging systematics, and spectroscopic efficiency are accounted for using additional weights as described in [40]. As imaging systematics are crucial to this analysis, the imaging systematics weights are further improved using the regression code REGRESSIS [26,41]. However, as shown in Fig. 25 of [26], the systematic weights primarily affect super-equality-horizon scales for the DESI QSO and LRG samples. This indicates that the α_{TO} measurement is robust against imaging systematics. However, imaging systematics can flatten the power spectrum at these scales or even cause an upturn,

³https://github.com/dfm/emcee.

⁴https://github.com/cosmodesi//blob/main/nb/turnover_examples.ipynb.

https://www.legacysurvey.org/dr9/.

⁶https://github.com/echaussidon/regressis.

which may result in an underestimation of the slope parameter m and, in turn, we might be prone to underestimating our detection probability.

We avoid confirmation bias by first testing and performing our analysis on blinded data. The blinding strategy and its validation is described in detail in [42,43]. DESI is blinded at the catalog level. At ultralarge scales, the dominant blinding contribution comes from imposing a randomly chosen value of $f_{\rm NL}^{\rm blind}$ \in [-15, 15]onto a set of weights such that one will measure $f_{\rm NL}^{\rm obs}=f_{\rm NL}^{\rm cat}+f_{\rm NL}^{\rm blind},$ where $f_{\rm NL}^{\rm cat}$ is the local PNG parameter measured from the unblinded catalog. To prevent unblinding without knowing $f_{\rm NL}^{\rm blind}$, the completeness weights available to the collaboration before unblinding were multiplied by the blinding weights. The blinded power spectrum is shown in pale along their unblinded equivalents in Fig. 3. We show in Sec. IV D using mocks that the f_{NL} blinding strategy is also efficient for this turnover analysis.

Being commensal with the DESI PNG analysis [26], our power spectra have been obtained using the Yamamoto estimator [44] implemented in PYPOWER⁷ even though we only consider the power spectrum monopole here. FKP weights [39]

$$w_{\text{FKP}}(\mathbf{x}) = \frac{1}{1 + \bar{n}(\mathbf{x})P_0} \tag{16}$$

are applied to minimize the uncertainty of the power spectrum measurement, where P_0 is the power spectrum at the scale of interest. With the equality scale as our scale of interest, $P_0 = 3 \times 10^4 \; \mathrm{Mpc^3}/h^3$ and $P_0 = 5 \times 10^4 \; \mathrm{Mpc^3}/h^3$ are chosen for the QSO and LRG power spectrum measurement, respectively. PYPOWER automatically subtracts Poissonian shot noise. Thus, our nuisance parameter $s_{n,0}$ presents the residual shot noise.

A. Mock realizations

We make use of two sets of simulations: EZmocks [46] and Abacus [47,48]. EZmocks use Gaussian random fields to initialize density perturbations in the early Universe. The evolution of these density perturbations is modeled under the assumption of the Zel'dovich approximation and an effective bias model, which is computationally less intensive than full N-body simulations. This methodology balances computational efficiency and accuracy, particularly on these ultralarge scales that can be well described by linear theory, allowing the creation of 1000 realizations per galactic hemisphere with a box size of $(6 \text{ Gpc/}h)^3$. We use two sets of realizations of EZmocks. For most applications, we use the mocks described in detail in Sec. 3.3.2 of [26].

When estimating correlations with other DESI measurements, in particular the BAO, we use EZmock realizations described in Sec. 3.2 of [11].

Abacus mocks are constructed on the foundation of the AbacusSummit simulations [47,48], a state-of-the-art set of cosmological N-body simulations that use an advanced GPU-accelerated codebase. These simulations are designed to produce high-resolution outputs for large cosmological volumes, making them particularly suited for DESI's vast survey footprint and stringent statistical requirements. With up to trillions of particles, AbacusSummit enables precise modeling of the dark matter density field and the resulting halo distribution. The simulations cover volumes comparable to or larger than the DESI survey, ensuring that cosmic variance is minimized and rare structures are wellsampled. Abacus mocks incorporate advanced halo modeling techniques, such as the halo occupation distribution (HOD), to populate halos with galaxies consistent with DESI's target selection. Due to their higher computational cost, we only have 25 Abacus mocks each with a box size of $(2 \text{ Gpc}/h)^3$ available.

B. The covariance matrix

To obtain the covariance matrix of the power spectrum, we repeat all steps initially taken to compute the data power spectra and apply them to all 1000 EZmock realizations that have also been used in the covariance estimation for the DESI PNG analysis [26]. This process yields the power spectrum $P_s(k)$ for each simulation s, with the average denoted as $\bar{P}(k)$. We compute the sample covariance with the formula

$$C_{\text{samp}}(k,q) = \frac{\sum_{s} [P_{s}(k) - \bar{P}(k)][P_{s}(q) - \bar{P}(q)]}{n_{\text{m}} - 1}$$
(17)

where $n_{\rm m}=1000$ represents the number of mock realizations. This provides an unbiased estimate of the true covariance matrix $C_{\rm true}(k_1,k_2)$. Given that the inverse covariance matrix follows an inverse Wishart distribution, $C_{\rm samp}^{-1}(k_1,k_2)$ is only a biased estimate of $C_{\rm true}^{-1}(k_1,k_2)$. To obtain an unbiased estimate, we multiply $C_{\rm samp}^{-1}(k_1,k_2)$ by the Hartlap factor [49]

$$C_{\rm H}^{-1}(k_1, k_2) = \frac{n_{\rm m} - n_{\rm d} - 2}{n_{\rm m} - 1} C_{\rm samp}^{-1}(k_1, k_2),$$
 (18)

where $n_{\rm d}$ is the number of data points. Furthermore, when using $C_{\rm H}^{-1}(k_1,k_2)$ instead of the unknown $C_{\rm true}(k_1,k_2)$ in any parameter inference, the likelihood becomes wider due to the marginalization over possible values of $C_{\rm true}(k_1,k_2)$. This effect can approximately be accounted for by the Percival factor [50]

⁷https://github.com/cosmodesi/pypower, based on [45].

$$C_{\rm PH}^{-1}(k_1, k_2) = \frac{2 + (n_{\rm m} - n_{\rm d} - 1)(n_{\rm m} - n_{\rm d} - 4) + (n_{\rm m} - n_{\rm d} - 2)(n_{\rm p} + 1)}{(n_{\rm m} - n_{\rm d} - 1)(n_{\rm m} - n_{\rm d} - 4) + (n_{\rm m} - n_{\rm d} - 2)(n_{\rm d} - n_{\rm p})} C_{\rm H}^{-1}(k_1, k_2), \tag{19}$$

where $n_{\rm p}=5$ is the number of parameters. Finally, we substitute $C_{\rm true}$ with $C_{\rm PH}$ in Eq. (14) to obtain the covariance matrix used to measure the turnover.

Note that in the DESI full shape analysis [37], the covariance matrix from the EZmocks is rescaled to match the analytical prediction from RascalC [51]. This is necessary as the EZmocks used in [37] emulate the fiber assignment of DESI, which in turn underestimates the covariance. Here, we use the EZmocks of the DESI PNG measurement [26], which ignore the impact of the fiber assignment. While this introduces inaccuracies at small scales that are not relevant for us, it has been shown that it does not underestimate the covariance [26].

C. The window matrix and the radial integral constraints

In power spectrum measurements, a window matrix formalism usually accounts for the survey's geometry, masked regions, and incompleteness, ensuring accurate modeling of the power spectrum [52]. The survey selection function, W(x), describes the observed fraction of the density field. The convolved power spectrum is computed as a matrix multiplication between the unconvolved power spectrum multipoles and the window matrix, as expressed in Eq. (4.8) of the DESI PNG paper [26].

We make again use of the window matrix of Ref. [26]. For the monopole ($\ell=0$), the window matrix is derived using the random catalog and normalized appropriately to avoid bias. The implementation utilizes PYPOWER for computing the window matrix and DESILIKE for the convolution with the theoretical model. Wide-angle corrections are included in the window matrix at first order.

The redshift distribution used to generate random catalogs is typically inferred directly from the data catalog using the shuffling method. This approach nulls radial modes in the measured power spectrum, leading to the radial integral constraint (RIC, [53]), which introduces anisotropic and scale-dependent effects. The DESI PNG paper [26] quantifies this contribution through an additive correction to the power spectrum or a multiplicative modification to the window function, $W \to W - W^{\rm RIC}$, ensuring that the RIC is properly accounted for without biasing the measurement of $f_{\rm NL}^{\rm loc}$.

Reference [26] demonstrated that the RIC correction affects both the monopole and quadrupole, with a suppression of power on large scales that can bias $f_{\rm NL}^{\rm loc}$ measurements if not corrected. For the monopole, this effect can be modeled by decreasing the effective value of

 $f_{\rm NL}^{\rm loc}$. The validity of this correction for $f_{\rm NL}^{\rm loc}$ has been confirmed using 100 pairs of mock catalogs with shuffled and unshuffled randoms and through a blinded procedure, validating its robustness across different power spectrum shapes. Using the same set of shuffled and unshuffled mock realizations as Ref. [26], we tested that the position of TO is unaffected by the RIC. However, the RIC affects the slope m of superequality-horizon scales and the uncertainty of $\alpha_{\rm TO}$. Hence, we adopt the RIC corrected window matrix from the DESI PNG analysis [26].

Finally, since the covariance matrix obtained from shuffled mocks is consistent with that derived from unshuffled mocks, we can estimate the covariance from the full set of 1000 unshuffled mocks. These steps ensure that both the window matrix and RIC effects are correctly incorporated, allowing for unbiased parameter inference in our analysis.

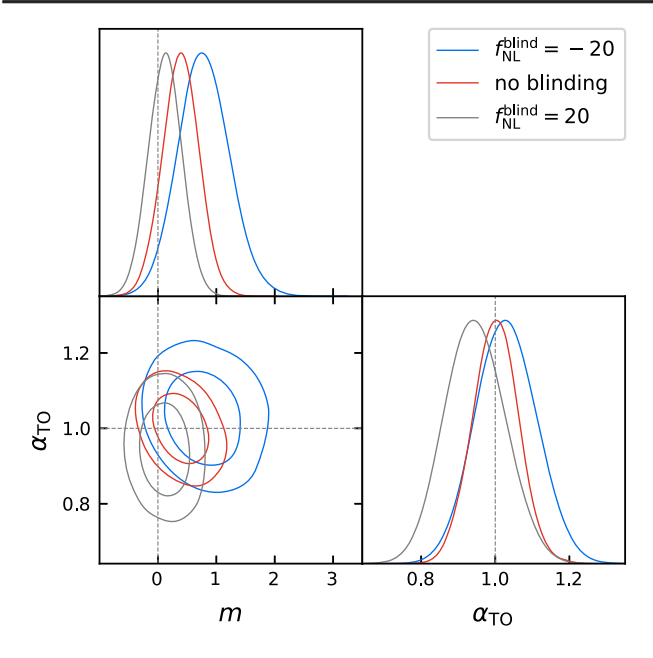
D. Validation of blinding

The DESI blinding strategy [42,43] was not designed with a turnover measurement in mind. However, the turnover scale lies between the scales relevant for the PNG analysis and the BAO scale, so, here, we test whether the blinding developed for these measurements also blinds the turnover measurement. Values of $f_{\rm NL}^{\rm loc}$ that are consistent with Planck 18 data [54] only cause subpercent shifts in the turnover scale [55]. However, the DESI blinding allows for three times larger values, making the bias already scale-dependent at the turnover scale.

Using a set of mocks generated from a single Abacus realization but with different values of $f_{\rm NL}^{\rm blind}$, $w_0^{\rm blind}$ and $w_a^{\rm blind}$, we measure the m, n, $\alpha_{\rm TO}$, b_1 , and $s_{n,0}$ posterior distributions of each mock, as shown in Fig. 4 for variation in $f_{\rm NL}^{\rm blind}$. We do not see any significant change in the best-fitting parameters as $w_0^{\rm blind}$ and $w_a^{\rm blind}$ are changed. Nonetheless, the PNG blinding works well also for the turnover measurement presented in this work.

E. Correlation between quasar and luminous red galaxies samples

The LRG and QSO samples overlap in the redshift range of 0.8 < z < 1.1. To perform joint inference using the turnover measurement from both samples, we need to estimate the correlation between the two samples. We can model the cross-power spectrum between two samples as



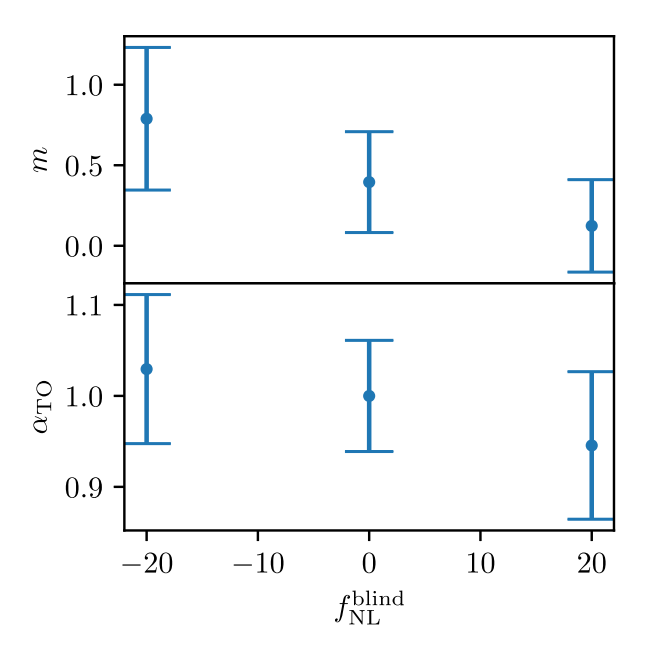


FIG. 4. Top: α_{TO} -m contours obtained from the same Abacus LRG mock without any blinding applied (red), and with a blinding corresponding to $f_{\text{NL}}^{\text{blind}} = \pm 20$ applied. Bottom: the dependence of the best-fitting values of m and α_{TO} and their uncertainties as a function of $f_{\text{NI}}^{\text{blind}}$.

$$P_{ij}(k) = \frac{\int dz \, p_i(z) p_j(z) P_{\rm m}(k, z)}{\int dz n_i(z) \int dz n_j(z)},$$
 (20)

with $p_i(z) = n_i(z)K_i(z)$, and $n_i(z)$ and $K_i(z)$ denoting the number density and Kaiser factor [cf. below Eq. (12)] of tracer i at redshift z, as well as $P_m(k)$ being the underlying matter power spectrum which is common to both tracers. A rough estimate for the correlation between the two samples can be obtained by

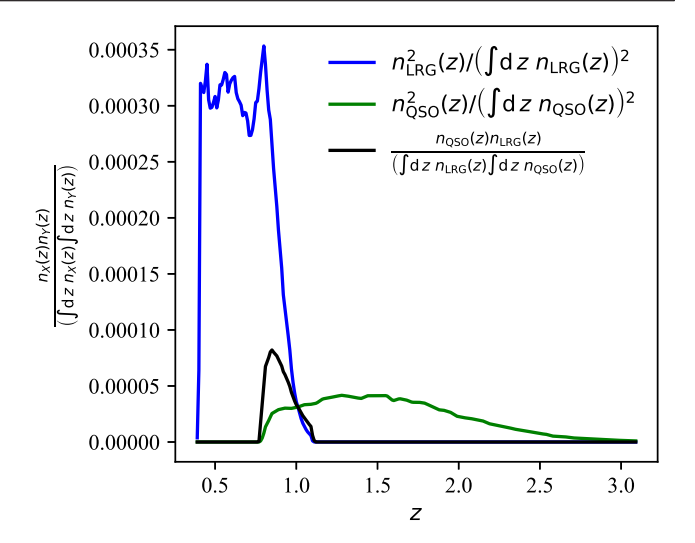


FIG. 5. Products of the normalized redshift distributions of the LRG and QSO samples.

$$\rho = \frac{P_{\text{LRG,QSO}}(k)}{\sqrt{P_{\text{LRG}}(k)P_{\text{QSO}}(k)}}
= \frac{\int dz \, p_{\text{LRG}}(z)p_{\text{QSO}}(z)D^{2}(z)}{\sqrt{\int dz \, p_{\text{LRG}}^{2}(z)D^{2}(z)}\sqrt{\int dz \, p_{\text{QSO}}^{2}(z)D^{2}(z)}}, \quad (21)$$

where we used $P_{\rm m}(k,z) = D^2(z)P_{\rm m}(k,0)$ in the second equality. Adopting the redshift distributions from [26], illustrated in Fig. 5, we evaluate Eq. (21) and find a percent-level correlation between the LRG and QSO clustering. The full impact on the measurement of α_{TO} would be best estimated in mock data. However, the EZmocks built for the sample selections used in [26] and this work are obtained from different realizations of the underlying matter density field. We, thus, make the conservative choice of estimating the correlation between the LRG and QSO α_{TO} measurements from the EZmock realizations used in the DESI direct tracer BAO analysis [11]. This is conservative because the QSO BAO mocks only extend up to redshift z = 2.1 and not z = 3.1 as in this analysis. When computing the sample covariance, we find a small correlation coefficient of 0.062, which we include in the cosmological parameter estimation presented in Sec. V C. The correlation matrix, along with BAO parameter correlations, is presented in Fig. 7.

V. RESULTS

A. Measurement of the turnover scale

We present the model-independent results of our turnover measurement in Table I. The power spectrum can be parametrized well around the turnover by the modelindependent parametrization of Eq. (12) as we find $\chi^2_{\rm min} =$ 81.2 and $\chi^2_{\rm min} =$ 112.8 from the QSOs and LRGs,

TABLE I. Best-fitting parameter values and 1σ quantiles for the slope parameter m, as well as the turnover dilation parameter α_{TO} , and the detection probability $\mathcal{P}_{\text{det}} = \mathcal{P}(m > 0)$. For m, we also list the posterior mean in brackets.

	m	\mathcal{P}_{det} (%)	$lpha_{ ext{TO}}$	$\frac{\chi^2_{\min}}{d.o.f}$
QSO	$0.68(0.74) \pm 0.41$	98	$\begin{array}{c} 1.049 \pm 0.067 \\ 0.988 \pm 0.047 \end{array}$	0.92
LRG	$0.23(0.28) \pm 0.25$	90		1.28

respectively. Having used 93 k-bins in both fits and with 5 free parameters, this corresponds to a reduced χ^2 of 0.92 from the QSOs and 1.28 from the LRGs. After unblinding, we detect the turnover with a 90% probability in the LRG power spectrum and a 98% probability in QSO data. These probabilities are estimated as the posterior volume with $\mathcal{P}(m>0)$. We show the α_{TO} -m posterior contours and their respective marginalized 1D distributions in Fig. 6. As the m posterior distribution is non-Gaussian with a pronounced tail toward large positive values, we also list the m posterior means in Table I alongside its best-fitting value. We notice that the contours have shrunk after unblinding, a behavior we also observe in the mocks (cf. Fig. 4). In both cases, the goodness of fit has increased as well, with $\chi^2_{\min} = 100.0$ from the blinded QSO sample and $\chi^2_{\rm min}=156.5$ from the blinded LRG sample. In any case, as we can see in Fig. 3, the unblinded power spectra are enhanced around the turnover, making it easier to detect. Our best-fitting values of the turnover scale parameter are $\alpha_{TO} = 1.049 \pm 0.067$ from the QSO sample and $\alpha_{TO} = 0.988 \pm 0.047$ from the LRGs, in either case, consistent with $\alpha_{TO} = 1$, and, in turn, with the fiducial cosmological model.

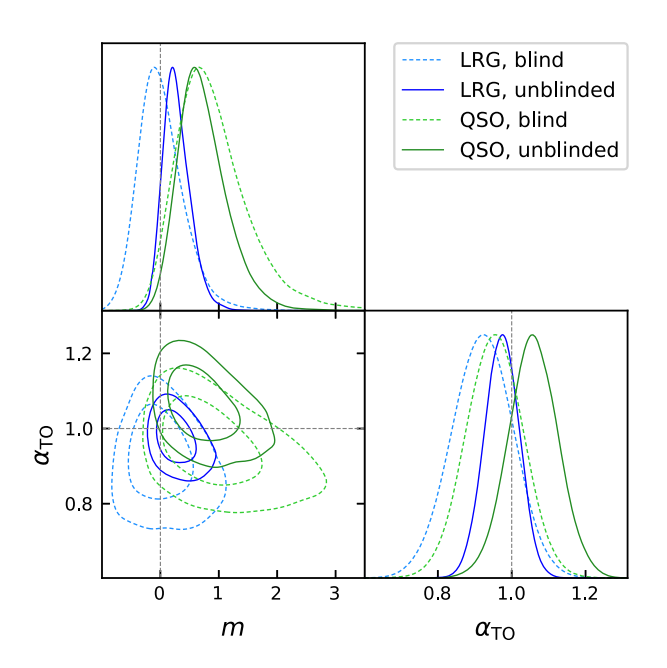


FIG. 6. α_{TO} -m contours from the blind (dashed) and unblinded (solid) LRG and QSO catalogs.

B. Correlation between turnover and BAO measurements

A measurement of α_{TO} can be translated into a highly degenerate measurement of $\Omega_{\rm m}$ and H_0 . One way to break this degeneracy while remaining agnostic about the sound-horizon scale $r_{\rm d}$ is to incorporate $\Omega_{\rm m}$ information from the BAO. In the eBOSS analysis [2], we measured the turnover from QSOs only and combined this measurement with BAO measurements from the Lyman- α forest and tracers other than QSOs to avoid correlations between the two datasets. Since we are measuring the turnover from LRGs here, we would also lose a considerable amount of constraining power if we were disregarding the DESI LRG and OSO BAO constraints.

This is why we use again the EZmock best-fitting values of α_{TO} from Sec. IV E and correlate them with the best-fitting BAO parameters α_{iso} and α_{AP} from the same mocks used in the covariance estimation for the main DESI BAO analysis [11]. We do not consider the BAO from the DESI Lyman- α analysis [12] as it would be more complicated to estimate its correlation with the turnover measurement given that we use QSOs that have been used in the Lyman- α analysis.

We illustrate the turnover-BAO correlations also in Fig. 7. All these correlations are weaker than the correlation between the QSO and LRG turnover parameters. The most significant turnover-BAO (anti)correlation occurs between QSOs and isotropic LRG BAO in the redshift bin of 0.4 < z < 0.6. Since these represent different populations in nonadjacent redshift bins, we consider this and all other

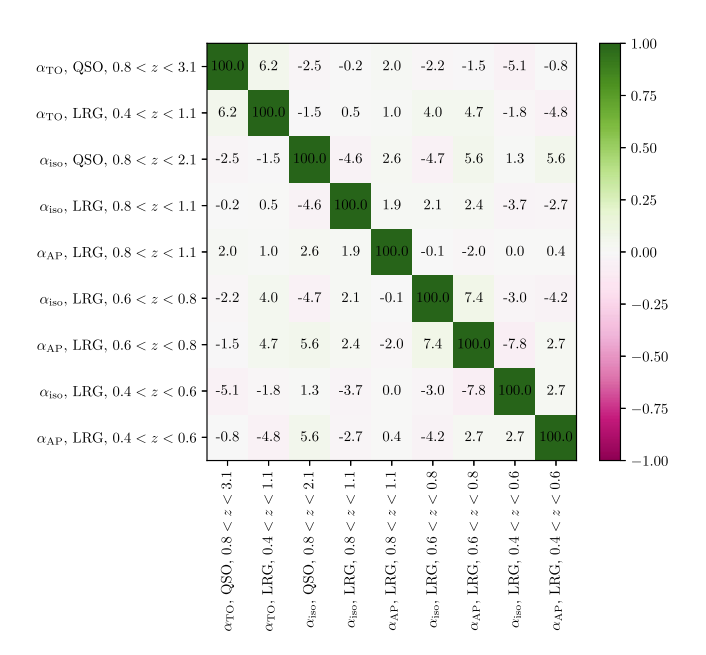


FIG. 7. Correlations in percentage between α_{TO} , as well as postreconstruction α_{iso} and α_{AP} for the QSO and LRG samples in percent. These correlation matrices have been estimated from 1000 EZmocks. We also show the correlations between the QSO and LRG α_{TO} , as they overlap in redshift.

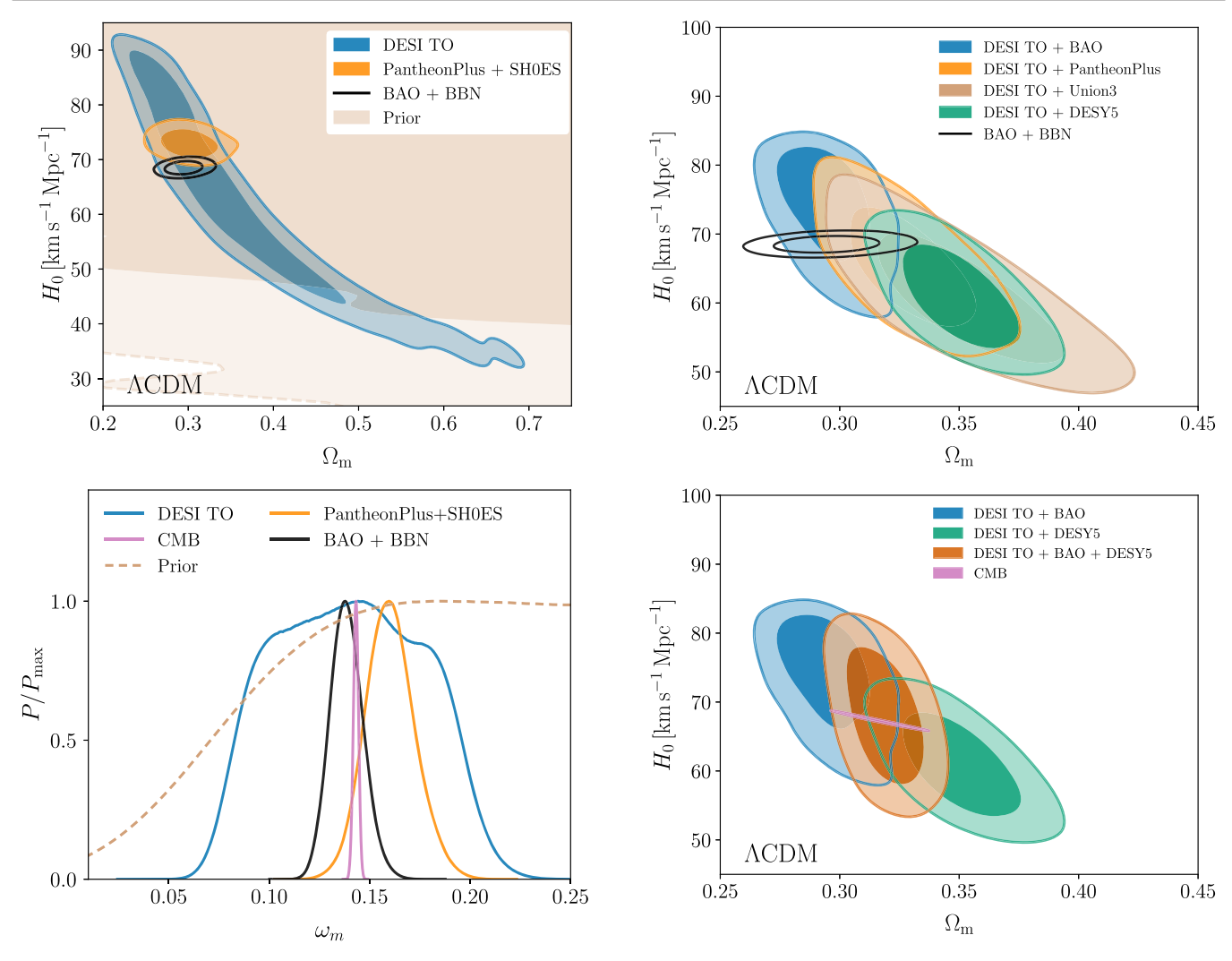


FIG. 8. Constraints on the Λ CDM parameters H_0 and $\Omega_{\rm m}$ (top), as well as $\omega_{\rm m}$ (bottom) using DESI turnover measurement (blue). These are compared to constraints from PantheonPlus + SH0ES (yellow), DESI BAO + BBN (black), and Planck (magenta, bottom panel only). Priors are imposed on $\omega_{\rm b}$ and $\omega_{\rm cdm}$. To illustrate how these priors translate into priors on H_0 , $\Omega_{\rm m}$ and $\omega_{\rm m}$, we randomly sample points from the priors and include their contours in gold.

less correlated pairs to be coincidental correlations and thus treat them as independent.

Additionally, DESI provides a further model-independent approach to obtain information beyond BAO and RSD parameters, the ShapeFit approach [56,57], which, however, has not been used for cosmological parameter estimation [37]. We investigate the correlation between turnover measurements and ShapeFit parameters in Appendix B.

C. The turnover scale as a standard ruler

We have presented a model-independent measurement of the power spectrum turnover scale in Table I. As outlined in

FIG. 9. Top: $\Omega_{\rm m}$ - H_0 posterior contours when combining the DESI turnover measurement with either the DESI BAO, or SN constraints from PantheonPlus [59,60], Union3 [61], and DESY5 [62]. Bottom: similar to top panel exploring combinations of TO, BAO, and SNe and comparing those with CMB constraints.

Sec. III A, we can use this measurement as a standard ruler to make inferences on a particular cosmological model. We begin with a basic flat Λ CDM model, wherein H(z) is defined by H_0 and $\Omega_{\rm m}$ at lower redshifts, and by H_0 , $\Omega_{\rm r}$, and $\Omega_{\rm m}$ through to the matter-radiation equality epoch. By using Eqs. (2)–(5) and fixing the mean CMB temperature at $T_{\gamma}=(2.72548\pm0.00057)~{\rm K}$ [58], $\Omega_{\rm r}$ effectively becomes dependent solely on H_0 . Consequently, we sample the H_0 - $\Omega_{\rm m}$ posterior contour represented in blue in Fig. 8. These contours are degenerate, hindering competitive constraints on either H_0 or $\Omega_{\rm m}$ independently. Nonetheless, as illustrated at the bottom of Fig. 8, we can sample instead $\omega_{\rm m} \equiv \Omega_{\rm m} h^2$ to obtain a CMB anisotropy-independent constraint of

$$\Omega_{\rm m}h^2 = 0.139 \pm 0.036. \tag{22}$$

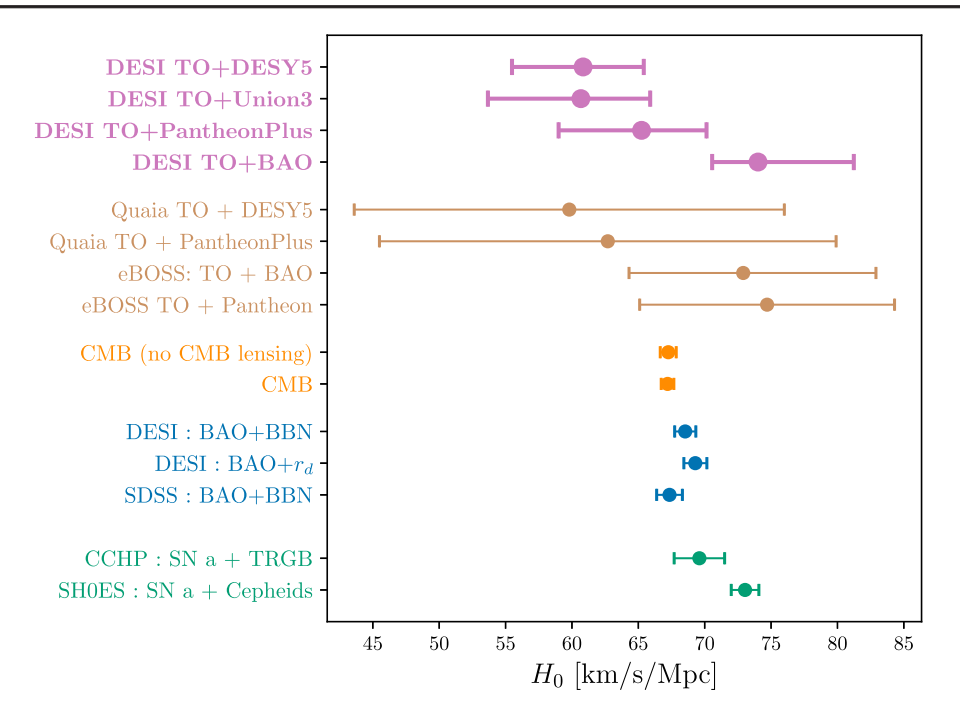


FIG. 10. Whisker plot comparing the Λ CDM H_0 constraints from DESI TO and the external datasets employed in this work (purple) with other TO based constraints (brown), CMB constraints (orange), BAO constraints obtained with BBN or CMB r_d priors (blue), and SN distance ladder results (green).

This result aligns with $\Omega_{\rm m}h^2=0.159^{+0.041}_{-0.037}$ derived from the eBOSS QSO turnover measurement [2,23] and $\Omega_{\rm m}h^2=0.1430\pm0.0011$ obtained from the Planck mission [21].

One of the motivations for measuring the turnover was obtaining a sound-horizon-free measurement of the Universe's expansion rate H_0 . One way to achieve this

by relying entirely on DESI data is to break the turnover H_0 - $\Omega_{\rm m}$ degeneracy. This can be done with uncalibrated anisotropic BAO measurements, which provide independent constraints on $\Omega_{\rm m}$. We show our joint $\Lambda{\rm CDM}~\Omega_{\rm m}$ - H_0 posterior distribution in Fig. 9 from which we obtain a marginalized mean value of $H_0 = 74.0^{+7.2}_{-3.5}~{\rm km/s/Mpc}$.

TABLE II. The results for cosmological parameters from turnover measurements, combined with external datasets and priors, are presented within the baseline flat Λ CDM model and its w_0w_a extension. We report marginalized means and 68% credible intervals.

Model/dataset	$\Omega_{ m m}$	$H_0 \text{ [km s}^{-1} \text{ Mpc}^{-1}\text{]}$	ω_m	w_0	w_a
Flat ACDM					
DESI TO	$0.354^{+0.030}_{-0.11}$	65^{+20}_{-10}	0.139 ± 0.036		
DESI TO $+$ BAO	0.295 ± 0.013	$74.0_{-3.5}^{+7.2}$	$0.162^{+0.027}_{-0.017}$		
DESI TO + PantheonPlus	0.329 ± 0.018	$65.2^{+4.9}_{-6.2}$	$0.140^{+0.017}_{-0.023}$		
DESI TO + Union3	0.353 ± 0.026	$60.7^{+5.2}_{-7.0}$	$0.130^{+0.016}_{-0.023}$		
DESI TO + DESY5	0.350 ± 0.017	$60.8^{+4.6}_{-5.4}$	$0.130^{+0.016}_{-0.020}$		
DESI $TO + BAO + PantheonPlus$	0.308 ± 0.011	$70.7^{+7.7}_{-5.9}$	0.155 ± 0.026		
DESI $TO + BAO + Union3$	$0.308^{+0.011}_{-0.013}$	$71.0_{-5.5}^{+7.8}$	$0.156^{+0.030}_{-0.024}$		
$DESI\ TO + BAO + DESY5$	0.319 ± 0.011	67.9 ± 6.3	$0.148^{+0.024}_{-0.029}$		
CMB	0.3165 ± 0.0084	67.27 ± 0.60	0.1432 ± 0.0013		
Flat $w_0 w_a CDM$					
DESI TO	$0.374^{+0.060}_{-0.16}$	63^{+20}_{-10}	$0.140^{+0.021}_{-0.058}$	$-0.90^{+1.0}_{-0.86}$	< -0.560
DESI TO $+$ BAO	$0.344^{+0.039}_{-0.029}$	66.5 ± 7.2	0.152 ± 0.026	$-0.53^{+0.38}_{-0.22}$	< -1.32
DESI $TO + BAO + PantheonPlus$	$0.311^{+0.012}_{-0.014}$	70^{+8}_{-5}	$0.155^{+0.030}_{-0.022}$	-0.865 ± 0.073	$-0.56^{+0.51}_{-0.39}$
DESI $TO + BAO + Union3$	0.331 ± 0.015	67^{+8}_{-6}	$0.151^{+0.031}_{-0.026}$	-0.66 ± 0.12	$-1.35^{+0.68}_{-0.59}$
DESI $TO + BAO + DESY5$	0.324 ± 0.014	68^{+8}_{-6}	$0.150_{-0.027}^{+0.029}$	-0.738 ± 0.087	$-1.11^{+0.57}_{-0.51}$
BAO + CMB + DESY5	0.3163 ± 0.0066	67.23 ± 0.66	0.1429 ± 0.0011	-0.726 ± 0.070	$-1.06^{+0.35}_{-0.29}$

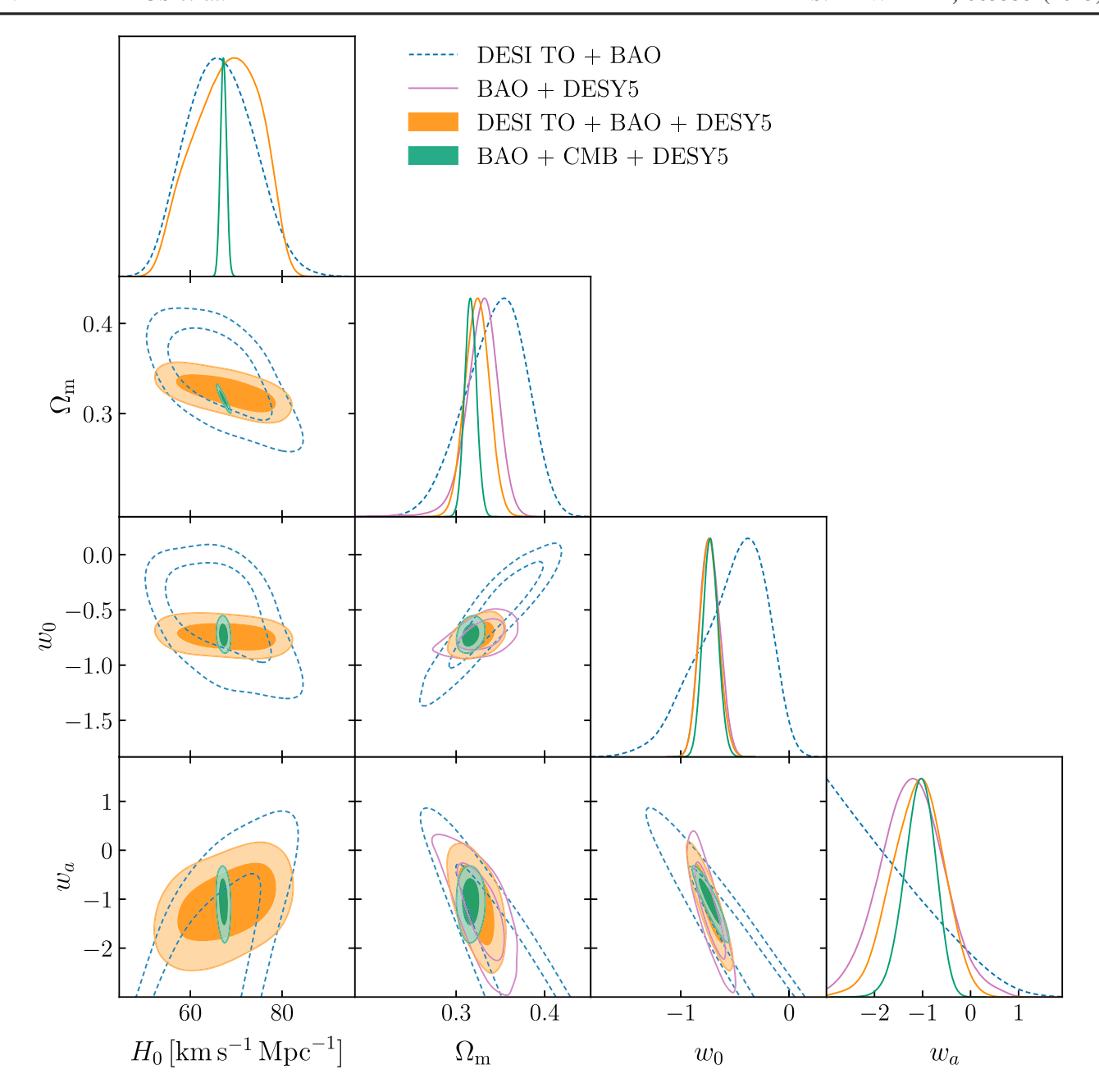


FIG. 11. Posterior contours for H_0 , $\Omega_{\rm m}$, and the dark energy parameters w_0 and w_a . Note, that we do not show any H_0 contours for BAO + DESY5 as these are $r_{\rm d}$ dependent [13].

This is almost 2σ higher than the Planck CMB value of $H_0=67.27\pm0.60$ [21]. It is also higher than BAO H_0 measurements with sound-horizon priors from either big bang nucleosynthesis (BBN) or from the CMB (cf. Fig. 10) but it is consistent with the 71.2 ± 4.1 km/s/Mpc-measurement from the DESI galaxy clustering only full-shape analysis where the sound horizon has been marginalized out [14], as well as the eBOSS TO + BAO and eBOSS TO + Pantheon results [2,23].

Our DESI TO + BAO result is also close to the SH0ES measurement of $H_0 = 73.04 \pm 1.04$ km/s/Mpc [63] which we also add to the whisker plot in Fig. 10 for

comparison, showing a clear visualization of how our results compare to previous measurements. As SNe also provide a direct measurement of $\Omega_{\rm m}$ but a H_0 measurement that is degenerate with intrinsic properties of SNe, we also combine our DESI TO constraints with the SN likelihoods considered in the DESI cosmological parameter inference key articles [13,37], which are the PantheonPlus⁸ [59,60], Union3 [61], and the Year 5 SN analysis from the Dark

⁸As in [37], we denote the originally named Pantheon+ dataset henceforth as PantheonPlus to avoid ambiguity with the + symbol used to denote combinations of datasets.

Energy Survey (DESY5) [62]. Interestingly, our analysis indicates an inverse Hubble tension. The DESI TO + Union3 and DESI TO + DESY5 combinations yield significantly lower values of H_0 at $60.7^{+5.2}_{-7.0}$ km/s/Mpc and $60.8^{+4.6}_{-5.4}$ km/s/Mpc, respectively, compared to our DESI TO + BAO constraints (see Table II and Figs. 9 and 10). When combining with the PantheonPlus dataset, we observe a milder tension, resulting in a marginalized mean and 68% credible interval of $H_0 = 65.2^{+4.9}_{-6.2}$ km/s/Mpc. It is important to note that this inverse Hubble tension is not indicative of an inconsistency within the DESI TO constraints. Instead, it reflects the differences in the values of $\Omega_{\rm m}$: 0.295 \pm 0.015 from DESI BAO [13] versus 0.356 $^{+0.028}_{-0.026}$ from Union3 [61], to give as an example the datasets that result in the highest tension when combining with the DESI TO.

This $\Omega_{\rm m}$ tension can be resolved by allowing for evolving dark energy. In this model, DESI BAO constrains the matter density parameter at $\Omega_{\rm m}=0.344^{+0.047}_{-0.026}$ [13]. In fact, DESI BAO + CMB + SNe favor evolving dark energy over Λ CDM at the 2.5 σ , 3.5 σ , or 3.9 σ level depending on whether the SN sample is PantheonPlus, Union3, or DESY5 [13]. Adopting the Chevallier-Polarski-Linder (CPL, [64,65]) parametrization where the dark energy equation of state $w(a)=w_0+w_a(1-a)$ at scale factor a is defined by the present-day value w_0 and the linear evolution parameter w_a , we can see that in this w_0w_a CDM model, DESI TO + BAO provides an H_0 constraint of 66.5 \pm 7.2 km/s/Mpc that agrees well with DESI TO + SNe.

Furthermore, we compare in Fig. 11 the posterior contours of the data combination that provided the strongest evidence for evolving dark energy, i.e., DESIBAO + DESY5 + CMB, to that from replacing the CMB with the DESI TO. While the TO yields less information than the CMB, it still provides a valuable consistency check when combined with BAO and supernovae but without directly relying on the CMB. The TO + BAO + DESY5 combination achieves competitive constraints with $w_0 = -0.738 \pm 0.087$ and $w_a = -1.11^{+0.57}_{-0.51}$, which are not far from the full DESI + CMB + DESY5 combination $(w_0 = -0.726 \pm 0.070, w_a = -1.06^{+0.35}_{-0.29},$ cf. Fig. 11). This suggests that the turnover can serve as an independent low-redshift probe, offering cross-checks and robustness tests against CMB-driven cosmological models.

VI. SUMMARY

In this study, we present the first model-independent detection of the power spectrum turnover in an autopower spectrum using data obtained from DESI during its inaugural survey year, with a detection probability of 98% in the QSO sample and 90% in the LRG sample. The power spectrum turnover serves as a model-independent

measurement of the matter-radiation equality scale. Our analysis, conducted with strict data blinding techniques to mitigate confirmation bias, yields $D_{\rm V}(z=1.651)=(38.1\pm2.5)r_{\rm H}$ from the quasars and $D_{\rm V}(z=0.733)=(21.8\pm1.0)r_{\rm H}$ from the LRG sample. These turnover scales are a crucial feature in the matter power spectrum and serve as a standard ruler in cosmology, complementary to the BAO.

Assuming three standard neutrino species and a vanilla Λ CDM cosmology, these measurements allow us to derive a constraint on the matter density parameter $\Omega_{\rm m}h^2=0.139^{+0.036}_{-0.046}$. By combining this with low-redshift measurements from type-Ia supernovae data (PantheonPlus, Union3, and DESY5), we obtain an estimate of the Hubble-Lemaître parameter independent from BBN or CMB priors: $H_0=60.7^{+5.2}_{-7.0}~{\rm km/s/Mpc},~60.8^{+4.6}_{-5.4}~{\rm km/s/Mpc},~and~65.2^{+4.9}_{-6.2}~{\rm km/s/Mpc},~respectively,~which~aligns~with~previous~Quaia~+~Planck~turnover~analyses.$

Furthermore, incorporating DESI BAO results, we estimate $H_0 = 74.0^{+7.2}_{-3.5}$ km/s/Mpc, consistent with findings from DESI full-shape analyses that marginalize the sound-horizon scale [14]. Note that this value presents true constraints from DESI alone without any external data, whereas H_0 constraints from the BAO alone are either presented as $H_0r_{\rm d}$ or are broken with external data, such as in Fig. 8 where the H_0 - $r_{\rm d}$ degeneracy has been broken with external BBN priors. The apparent inversion of H_0 values between Fig. 8 on one hand and Figs. 9 and 10 on the other, is due to the exclusion of priors from BBN and SH0ES Cepheid host distances.

Notably, the (now inverted) discrepancy in H_0 arises due to differences in the matter density measured by supernovae compared to those measured by the DESI BAO. When allowing for evolving dark energy, these differences are reconciled with DESI TO+BAO providing $H_0=66.5\pm7.2$ km/s/Mpc. However, the constraints on H_0 become less stringent. This work underscores the capacity of the turnover scale as a robust cosmological probe, providing valuable insights into the dynamics of the Universe.

Importantly, this analysis only uses data from the first year of DESI, representing just half of the area of the expected final sample. With four more years of observations planned, the final DESI dataset will contain approximately three times the effective volume of the first year data [11], significantly enhancing statistical precision and constraining power. Additionally, there are substantial efforts in addressing emission line galaxy (ELG) systematics, which have prohibited including them in this analysis. The recent implementation of improved imaging calibrations will reduce systematic biases. These improvements pave the way for incorporating ELG samples into future turnover analyses, increasing the number of available tracers by 50%, and, in turn, establishing the power spectrum turnover as a competitive additional probe.

ACKNOWLEDGMENTS

B. B.-K. thanks Matilde Barberi-Squarotti for her help with GETDIST. B. B.-K. acknowledges support from INAF for the project "Paving the way to radio cosmology in the SKA Observatory era: synergies between SKA pathfinders/ precursors and the new generation of optical/near-infrared cosmological surveys" (CUP C54I19001050001). This research was conducted using multiple high-performance computing resources. In addition to the facilities acknowledged by the Dark Energy Spectroscopic Instrument (DESI) and Legacy Surveys, including the National Energy Research Scientific Computing Center (NERSC), a Department of Energy User Facility, some of the cosmological analysis for this specific work was supported by the Seondeok high-performance computing clusters at the Korea Astronomy and Space Science Institute. Finally, to address specific comments from the referee, this work also made use of Pleiadi [66,67], a computing infrastructure installed and managed by INAF-USCVIII, under the proposal Simulations and Analyses Across the Spectrum -Setting the Stage for Euclid-SKAO Synergies. This material is based upon work supported by the U.S. Department of Energy (DOE), Office of Science, Office of High-Energy Physics, under Contract No. DE-AC02-05CH11231, and by the National Energy Research Scientific Computing Center, a DOE Office of Science User Facility under the same contract. Additional support for DESI was provided by the U.S. National Science Foundation (NSF), Division of Astronomical Sciences under Contract No. AST-0950945 to the NSF National Optical-Infrared Astronomy Research Laboratory; the Science and Technology Facilities Council of the United Kingdom; the Gordon and Betty Moore Foundation; the Heising-Simons Foundation; the French Alternative Energies and Atomic Energy Commission (CEA); the Council of Humanities, Science Technology of Mexico (CONAHCYT); the Ministry of Science and Innovation of Spain (MICINN), and by the DESI Member Institutions: [68]. The DESI Legacy Imaging Surveys consist of three individual and complementary projects: the Dark Energy Camera Legacy Survey (DECaLS), the Beijing-Arizona Sky Survey (BASS), and the Mayall z-band Legacy Survey (MzLS). DECaLS, BASS and MzLS together include data obtained, respectively, at the Blanco telescope, Cerro Tololo Inter-American Observatory, NSF NOIRLab; the Bok telescope, Steward Observatory, University of Arizona; and the Mayall telescope, Kitt Peak National Observatory, NOIRLab. NOIRLab is operated by the Association of Universities for Research in Astronomy (AURA) under a cooperative agreement with the National Science Foundation. Pipeline processing and analyses of the data were supported by NOIRLab and the Lawrence Berkeley National Laboratory. Legacy Surveys also uses data products from the Near-Earth Object Wide-field Infrared Survey Explorer

(NEOWISE), a project of the Jet Propulsion Laboratory/ California Institute of Technology, funded by the National Aeronautics and Space Administration. Legacy Surveys was supported by: the Director, Office of Science, Office of High Energy Physics of the U.S. Department of Energy; the National Energy Research Scientific Computing Center, a DOE Office of Science User Facility; the U.S. National Science Foundation, Division of Astronomical Sciences: the National Astronomical Observatories of China, the Chinese Academy of Sciences and the Chinese National Natural Science Foundation. LBNL is managed by the Regents of the University of California under contract to the U.S. Department of Energy. The complete acknowledgments can be found at [69]. The authors are honored to be permitted to conduct scientific research on Iolkam Du'ag (Kitt Peak), a mountain with particular significance to the Tohono O'odham Nation.

Any opinions, findings, and conclusions or recommendations expressed in this material are those of the author(s) and do not necessarily reflect the views of the U.S. National Science Foundation, the U.S. Department of Energy, or any of the listed funding agencies.

DATA AVAILABILITY

The data that support the findings of this article are openly available [70,71].

APPENDIX A: TEST OF α_{TO} SCALING RELATION ON MOCKS

This appendix details the test of the scaling relation for α_{TO} given in Eq. (9) using mock galaxy catalogs. Figure 12 shows the residuals of this scaling relation as a function of cosmological parameters. The test involves generating mock data, computing the power spectrum, and fitting for the turnover scale. The use of mocks is necessary to test the impact of the fiducial cosmology.

- (1) Mock data generation: Mock galaxy catalogs were generated using MOCKFACTORY's Lagrangian-LinearMock routine, which first creates a linear density field with a DESI-like fiducial cosmology implemented in COSMOPRIMO. Then, it displaces particles from their Lagrangian grid positions using the first-order Lagrangian perturbation theory (LPT)—i.e., the Zel'dovich approximation. The fiducial parameters are
 - (i) Redshift: z = 1.5
 - (ii) Linear power spectrum from the DESI fiducial model
 - (iii) Number density: $\bar{n} = 10^{-3} h^3/\text{Mpc}^3$
 - (iv) Simulation box parameters: boxsize = 3500 Mpc/h, nmesh = 256

https://github.com/cosmodesi/mockfactory.

Poisson sampling was used to populate the density field with galaxies.

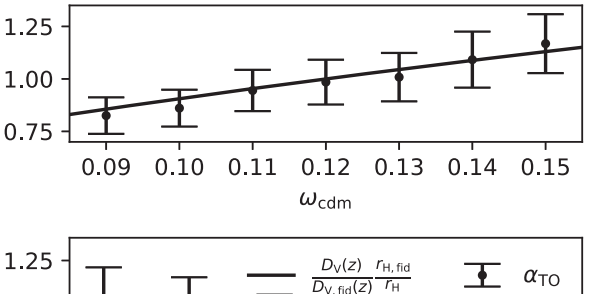
(2) Power spectrum computation: The power spectrum monopole was computed using pypower.CatalogFFTPower. Shot noise and normalization were accounted for. The covariance matrix was estimated assuming a Gaussian approximation

$$C(k_i, k_j) = \left[\frac{2}{V_n V_{\text{eff}}} P^2(k_i) + s_{n,0}^2\right] \delta_{ij}^{\text{K}}$$

where V_n are the Fourier-space volume elements. The effective volume, $V_{\rm eff}$, was calculated consistently with the main analysis.

- (3) Turnover scale fitting: The turnover scale, α_{TO} , was extracted from the mock power spectra using the same fitting pipeline described in the main text. Briefly, this involves fitting a model to the power spectrum around the turnover feature.
- (4) Testing the scaling relation: To assess the validity of the scaling relation in Eq. (9), we varied the values of $\omega_{\rm cdm}$ and h around the fiducial cosmology. For each variation:
 - (i) The fiducial cosmology used in Eq. (9) and when computing $r_{H,\text{fid}}$ remained fixed.
 - (ii) The mock power spectrum was recomputed using the updated cosmology.
 - (iii) The turnover scale, α_{TO} , was refitted.
 - (iv) α_{TO} was then compared to its prediction from Eq. (9), using r_{H} calculated for the varied cosmology.

The datapoints shown in Fig. 12 represent the left-hand side of Eq. (9), whereas the solid lines show the expectation from the right-hand side for these varied cosmologies.



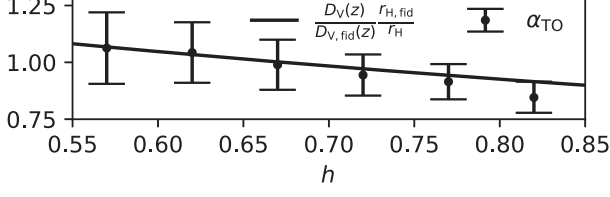


FIG. 12. Test of the α_{TO} scaling relation. Shown is the relative difference of the left- and right-hand sides of Eq. (9) as a function of ω_{cdm} and h. The data points correspond to α_{TO} from simulations, whereas the solid lines show the expectation from the right-hand side of Eq. (9). This demonstrates the validity of the scaling relation for a range of cosmological parameters.

APPENDIX B: CORRELATION WITH SHAPEFIT

Here, we analyze the correlation of the turnover parameters with ShapeFit parameters. ShapeFit extends the standard BAO and RSD measurements by including a parameter m_{SF} , which characterizes the shape of the power spectrum, and df, which accounts for deviations from standard growth predictions [56].

Using 1000 EZmock realizations, we estimate the correlation matrices between α_{TO} , α_{iso} , and α_{AP} pre and

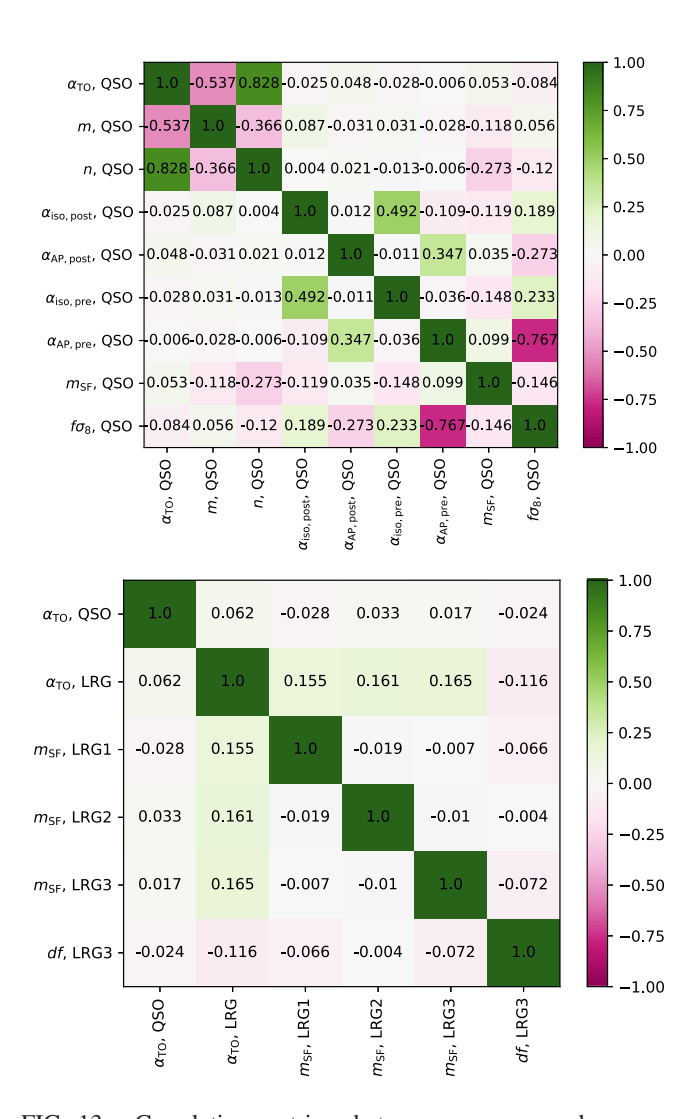


FIG. 13. Correlation matrices between $\alpha_{\rm TO}$, $\alpha_{\rm iso}$ and $\alpha_{\rm AP}$ pre and postreconstruction, as well as the ShapeFit parameter $m_{\rm SF}$ and df values for the QSO (left) and LRG (right) samples. These correlation matrices have been estimated from 1000 EZmocks. As the LRG sample is split into three redshifts bins for the BAO and ShapeFit analyses, we refer with LRG1, LRG2, and LRG3 to the redshift bins with 0.4 < z < 0.6, 0.6 < z < 0.8, and 0.8 < z < 1.1, respectively. We also show the correlations between the QSO and LRG $\alpha_{\rm TO}$, as they overlap in redshift. For clarity, in the right-hand panel, we only show parameters whose correlation with the LRG $\alpha_{\rm TO}$ is larger than 0.1.

postreconstruction, as well as m_{SF} and df for the QSO and LRG samples. These correlations are displayed in Fig. 13.

Since the LRG sample is split into three redshift bins for the BAO and ShapeFit analyses, we refer to these bins as LRG1 (0.4 < z < 0.6), LRG2 (0.6 < z < 0.8), and LRG3 (0.8 < z < 1.1). We also show the correlations between the QSO and LRG α_{TO} values due to their overlapping redshift range.

Overall, we find that the correlation between turnover and ShapeFit parameters is moderate, with the most significant correlations occurring between n and m_{SF} which is expected due to both parameters describing the power

spectrum shape at scales smaller than the turnover. In terms of α_{TO} , we do not see any strong correlations with ShapeFit parameters. This analysis suggests that incorporating ShapeFit parameters into joint fits may provide additional cosmological insights beyond standard BAO and turnover measurements since the shape parameter n is treated as a nuisance parameter in this analysis, whereas the related ShapeFit parameter m_{SF} is what provides additional information in the ShapeFit approach. It, therefore, seems worthwhile future work to combine the two parametrizations into a joint one, taking the information of both the turnover position and the slope of the power spectrum close to it into account.

- [1] G. B. Poole, C. Blake, D. Parkinson, S. Brough, M. Colless, C. Contreras *et al.*, The WiggleZ Dark Energy Survey: Probing the epoch of radiation domination using large-scale structure, Mon. Not. R. Astron. Soc. **429**, 1902 (2013).
- [2] B. Bahr-Kalus, D. Parkinson, and E.-M. Mueller, Measurement of the matter-radiation equality scale using the extended baryon oscillation spectroscopic survey quasar sample, Mon. Not. R. Astron. Soc. 524, 2463 (2023).
- [3] D. Alonso, O. Hetmantsev, G. Fabbian, A. Slosar, and K. Storey-Fisher, Measurement of the power spectrum turnover scale from the cross-correlation between CMB lensing and Quaia, arXiv:2410.24134.
- [4] A. Aghamousa, J. Aguilar, S. Ahlen, S. Alam, L. E. Allen et al. (DESI Collaboration), The DESI experiment part II: Instrument design, arXiv:1611.00037.
- [5] J. H. Silber, P. Fagrelius, K. Fanning, M. Schubnell, J. N. Aguilar, S. Ahlen *et al.*, The robotic multiobject focal plane system of the dark energy spectroscopic instrument (DESI), Astron. J. 165, 9 (2023).
- [6] T. N. Miller, P. Doel, G. Gutierrez, R. Besuner, D. Brooks, G. Gallo *et al.*, The optical corrector for the dark energy spectroscopic instrument, Astron. J. 168, 95 (2024).
- [7] C. Poppett, L. Tyas, J. Aguilar, C. Bebek, D. Bramall, T. Claybaugh *et al.*, Overview of the fiber system for the dark energy spectroscopic instrument, Astron. J. **168**, 245 (2024).
- [8] B. Abareshi, J. Aguilar, S. Ahlen, S. Alam, D. M. Alexander *et al.* (DESI Collaboration), Overview of the instrumentation for the dark energy spectroscopic instrument, Astron. J. 164, 207 (2022).
- [9] A. Aghamousa, J. Aguilar, S. Ahlen, S. Alam, L. E. Allen *et al.* (DESI Collaboration), The DESI experiment part I: Science, targeting, and survey design, arXiv:1611.00036.
- [10] M. Levi, C. Bebek, T. Beers, R. Blum, R. Cahn, D. Eisenstein *et al.*, The DESI experiment, a whitepaper for Snowmass 2013, arXiv:1308.0847.
- [11] A. G. Adame, J. Aguilar, S. Ahlen, S. Alam, D. M. Alexander *et al.* (DESI Collaboration), DESI 2024 III: Baryon acoustic oscillations from galaxies and quasars, J. Cosmol. Astropart. Phys. 04 (2025) 012.

- [12] A. G. Adame, J. Aguilar, S. Ahlen, S. Alam, D. M. Alexander *et al.* (DESI Collaboration), DESI 2024 IV: Baryon acoustic oscillations from the Lyman Alpha forest, J. Cosmol. Astropart. Phys. 01 (2025) 124.
- [13] A. G. Adame, J. Aguilar, S. Ahlen, S. Alam, D. M. Alexander *et al.* (DESI Collaboration), DESI 2024 VI: Cosmological constraints from the measurements of baryon acoustic oscillations, J. Cosmol. Astropart. Phys. 02 (2025) 021.
- [14] E. A. Zaborowski, P. Taylor, K. Honscheid, A. Cuceu, A. de Mattia, D. Huterer *et al.*, A sound horizon-free measurement of H₀ in DESI 2024, J. Cosmol. Astropart. Phys. 06 (2025) 020.
- [15] A. Krolewski, W. J. Percival, and A. Woodfinden, A new method to determine H_0 from cosmological energy-density measurements, Phys. Rev. Lett. **134**, 101002 (2025).
- [16] S. Brieden, H. Gil-Marín, and L. Verde, A tale of two (or more) h's, J. Cosmol. Astropart. Phys. 04 (2023) 023.
- [17] F. Prada, A. Klypin, G. Yepes, S. E. Nuza, and S. Gottloeber, Measuring equality horizon with the zero-crossing of the galaxy correlation function, arXiv:1111.2889.
- [18] F. Prada, E.-M. Mueller, B. Bahr-Kalus, R. Sheth, F. Nikakhtar, N. Padmanabhan, H. Zou, and N. Uberoi, Project: [383] Accurate Horizon-Size Measurement through Galaxy/QSO Correlation Zero-Crossing in DESI (to be published).
- [19] D. J. Eisenstein and W. Hu, Baryonic features in the matter transfer function, Astrophys. J. 496, 605 (1998).
- [20] D. Blas, J. Lesgourgues, and T. Tram, The cosmic linear anisotropy solving system (CLASS). Part II: Approximation schemes, J. Cosmol. Astropart. Phys. 07 (2011) 034.
- [21] N. Aghanim, Y. Akrami, M. Ashdown, J. Aumont, C. Baccigalupi *et al.* (Planck Collaboration), Planck 2018 results. VI. Cosmological parameters, Astron. Astrophys. **641**, A6 (2020).
- [22] N. Kaiser, Clustering in real space and in redshift space, Mon. Not. R. Astron. Soc. 227, 1 (1987).
- [23] B. Bahr-Kalus, D. Parkinson, and E.-M. Mueller, Correction to: Measurement of the matter-radiation equality scale using

- the extended baryon oscillation spectroscopic survey quasar sample, Mon. Not. R. Astron. Soc. **526**, 3248 (2023).
- [24] G. E. P. Box and D. R. Cox, An analysis of transformations, J. R. Stat. Soc.: Ser. B (Methodological) **26**, 211 (1964).
- [25] M. S. Wang, W. J. Percival, S. Avila, R. Crittenden, and D. Bianchi, Cosmological inference from galaxy-clustering power spectrum: Gaussianization and covariance decomposition, Mon. Not. R. Astron. Soc. 486, 951 (2019).
- [26] E. Chaussidon, C. Yèche, A. de Mattia, C. Payerne, P. McDonald, A. J. Ross *et al.*, Constraining primordial non-Gaussianity with DESI 2024 LRG and QSO samples, J. Cosmol. Astropart. Phys. 06 (2025) 029.
- [27] D. Foreman-Mackey, D. W. Hogg, D. Lang, and J. Goodman, emcee: The MCMC hammer, Publ. Astron. Soc. Pac. 125, 306 (2013).
- [28] A. D. Myers, J. Moustakas, S. Bailey, B. A. Weaver, A. P. Cooper, J. E. Forero-Romero *et al.*, The target-selection pipeline for the dark energy spectroscopic instrument, Astron. J. 165, 50 (2023).
- [29] D. Schlegel, A. Dey, D. Herrera, S. Juneau, M. Landriau, D. Lang et al., DESI legacy imaging surveys data release 9, in American Astronomical Society Meeting Abstracts, vol. 237 of American Astronomical Society Meeting Abstracts (2021), p. 235.03.
- [30] J. Guy, S. Bailey, A. Kremin, S. Alam, D. M. Alexander, C. Allende Prieto *et al.*, The spectroscopic data processing pipeline for the dark energy spectroscopic instrument, Astron. J. 165, 144 (2023).
- [31] C. Hahn, M. J. Wilson, O. Ruiz-Macias, S. Cole, D. H. Weinberg, J. Moustakas *et al.*, The DESI bright galaxy survey: Final target selection, design, and validation, Astron. J. **165**, 253 (2023).
- [32] R. Zhou, B. Dey, J. A. Newman, D. J. Eisenstein, K. Dawson, S. Bailey *et al.*, Target selection and validation of DESI luminous red galaxies, Astron. J. 165, 58 (2023).
- [33] A. Raichoor, J. Moustakas, J. A. Newman, T. Karim, S. Ahlen, S. Alam *et al.*, Target selection and validation of DESI emission line galaxies, Astron. J. **165**, 126 (2023).
- [34] E. Chaussidon, C. Yèche, N. Palanque-Delabrouille, D. M. Alexander, J. Yang, S. Ahlen *et al.*, Target selection and validation of DESI quasars, Astrophys. J. **944**, 107 (2023).
- [35] A. Rosado-Marin (DESI Collaboration), Mitigating imaging systematics for DESI DR1 emission line galaxies and beyond, J. Cosmol. Astropart. Phys. 07 (2025) 018.
- [36] A. J. Ross, J. Aguilar, S. Ahlen, S. Alam, A. Anand, S. Bailey *et al.*, The construction of large-scale structure catalogs for the dark energy spectroscopic instrument, J. Cosmol. Astropart. Phys. 01 (2025) 125.
- [37] A. G. Adame, J. Aguilar, S. Ahlen, S. Alam, D. M. Alexander *et al.* (DESI Collaboration), DESI 2024 VII: Cosmological constraints from the full-shape modeling of clustering measurements, J. Cosmol. Astropart. Phys. 07 (2025) 028.
- [38] A. J. Ross, J. Bautista, R. Tojeiro, S. Alam, S. Bailey, E. Burtin *et al.*, The completed SDSS-IV extended baryon oscillation spectroscopic survey: Large-scale structure catalogues for cosmological analysis, Mon. Not. R. Astron. Soc. **498**, 2354 (2020).

- [39] H. A. Feldman, N. Kaiser, and J. A. Peacock, Power-spectrum analysis of three-dimensional redshift surveys, Astrophys. J. **426**, 23 (1994).
- [40] A. J. Ross, J. Aguilar, S. Ahlen, S. Alam, A. Anand, S. Bailey *et al.*, The construction of large-scale structure catalogs for the dark energy spectroscopic instrument, arXiv:2405.16593.
- [41] E. Chaussidon, C. Yèche, N. Palanque-Delabrouille, A. de Mattia, A. D. Myers, M. Rezaie *et al.*, Angular clustering properties of the DESI QSO target selection using DR9 Legacy Imaging Surveys, Mon. Not. R. Astron. Soc. **509**, 3904 (2022).
- [42] E. Chaussidon, A. de Mattia, C. Yèche, J. Aguilar, S. Ahlen, D. Brooks *et al.*, Blinding scheme for the scale-dependence bias signature of local primordial non-Gaussianity for DESI 2024, J. Cosmol. Astropart. Phys. 01 (2025) 135.
- [43] U. Andrade, J. Mena-Fernández, H. Awan, A. J. Ross, S. Brieden, J. Pan *et al.*, Validating the galaxy and quasar catalog-level blinding scheme for the DESI 2024 analysis, J. Cosmol. Astropart. Phys. 01 (2025) 128.
- [44] K. Yamamoto, M. Nakamichi, A. Kamino, B. A. Bassett, and H. Nishioka, A measurement of the quadrupole power spectrum in the clustering of the 2dF QSO Survey, Publ. Astron. Soc. Jpn. **58**, 93 (2006).
- [45] N. Hand, Y. Li, Z. Slepian, and U. Seljak, An optimal FFT-based anisotropic power spectrum estimator, J. Cosmol. Astropart. Phys. 07 (2017) 002.
- [46] C.-H. Chuang, F.-S. Kitaura, F. Prada, C. Zhao, and G. Yepes, EZmocks: Extending the Zel'dovich approximation to generate mock galaxy catalogues with accurate clustering statistics, Mon. Not. R. Astron. Soc. **446**, 2621 (2015).
- [47] N. A. Maksimova, L. H. Garrison, D. J. Eisenstein, B. Hadzhiyska, S. Bose, and T. P. Satterthwaite, ABACUS-SUMMIT: A massive set of high-accuracy, high-resolution N-body simulations, Mon. Not. R. Astron. Soc. 508, 4017 (2021).
- [48] L. H. Garrison, D. J. Eisenstein, D. Ferrer, N. A. Maksimova, and P. A. Pinto, The ABACUS cosmological N-body code, Mon. Not. R. Astron. Soc. 508, 575 (2021).
- [49] J. Hartlap, P. Simon, and P. Schneider, Why your model parameter confidences might be too optimistic. Unbiased estimation of the inverse covariance matrix, Astron. Astrophys. **464**, 399 (2007).
- [50] W. J. Percival, A. J. Ross, A. G. Sánchez, L. Samushia, A. Burden, R. Crittenden *et al.*, The clustering of Galaxies in the SDSS-III Baryon Oscillation Spectroscopic Survey: Including covariance matrix errors, Mon. Not. R. Astron. Soc. **439**, 2531 (2014).
- [51] M. Rashkovetskyi, D. Forero-Sánchez, A. de Mattia, D. J. Eisenstein, N. Padmanabhan, H. Seo *et al.*, Semi-analytical covariance matrices for two-point correlation function for DESI 2024 data, J. Cosmol. Astropart. Phys. 01 (2025) 145.
- [52] F. Beutler and P. McDonald, Unified galaxy power spectrum measurements from 6dFGS, BOSS, and eBOSS, J. Cosmol. Astropart. Phys. 11 (2021) 031.
- [53] A. de Mattia and V. Ruhlmann-Kleider, Integral constraints in spectroscopic surveys, J. Cosmol. Astropart. Phys. 08 (2019) 036.

- [54] Y. Akrami, F. Arroja, M. Ashdown, J. Aumont, C. Baccigalupi *et al.* (Planck Collaboration), Planck 2018 results. IX. Constraints on primordial non-Gaussianity, Astron. Astrophys. 641, A9 (2020).
- [55] S. Cunnington, Detecting the power spectrum turnover with H I intensity mapping, Mon. Not. R. Astron. Soc. 512, 2408 (2022).
- [56] S. Brieden, H. Gil-Marín, and L. Verde, ShapeFit: Extracting the power spectrum shape information in galaxy surveys beyond BAO and RSD, J. Cosmol. Astropart. Phys. 12 (2021) 054.
- [57] A. G. Adame, J. Aguilar, S. Ahlen, S. Alam, D. M. Alexander *et al.* (DESI Collaboration), DESI 2024 V: Full-shape galaxy clustering from galaxies and quasars, J. Cosmol. Astropart. Phys. 09 (2025) 008.
- [58] D. J. Fixsen, The temperature of the cosmic microwave background, Astrophys. J. **707**, 916 (2009).
- [59] D. Scolnic, D. Brout, A. Carr, A. G. Riess, T. M. Davis, A. Dwomoh *et al.*, The Pantheon+ analysis: The full data set and light-curve release, Astrophys. J. 938, 113 (2022).
- [60] D. Brout, D. Scolnic, B. Popovic, A. G. Riess, A. Carr, J. Zuntz *et al.*, The Pantheon+ analysis: Cosmological constraints, Astrophys. J. 938, 110 (2022).
- [61] D. Rubin, G. Aldering, M. Betoule, A. Fruchter, X. Huang, A. G. Kim *et al.*, Union Through UNITY: Cosmology with 2,000 SNe using a unified bayesian framework, arXiv:2311.12098.
- [62] M. Vincenzi, D. Brout, P. Armstrong, B. Popovic, G. Taylor, M. Acevedo *et al.*, The dark energy survey supernova program: Cosmological analysis and systematic uncertainties, Astrophys. J. **975**, 86 (2024).
- [63] A. G. Riess, W. Yuan, L. M. Macri, D. Scolnic, D. Brout, S. Casertano et al., A comprehensive measurement of the

- local value of the Hubble constant with 1 km s⁻¹ Mpc⁻¹ uncertainty from the Hubble space telescope and the SH0ES team, Astrophys. J. Lett. **934**, L7 (2022).
- [64] M. Chevallier and D. Polarski, Accelerating universes with scaling dark matter, Int. J. Mod. Phys. D 10, 213 (2001).
- [65] E. V. Linder, Exploring the expansion history of the universe, Phys. Rev. Lett. 90, 091301 (2003).
- [66] G. Taffoni, U. Becciani, B. Garilli, G. Maggio, F. Pasian, G. Umana et al., CHIPP: INAF Pilot Project for HTC, HPC and HPDA, in Astronomical Data Analysis Software and Systems XXIX, edited by R. Pizzo, E. R. Deul, J. D. Mol, J. de Plaa, and H. Verkouter, Vol. 527 of Astronomical Society of the Pacific Conference Series (2020), p. 307, arXiv:2002.01283.
- [67] S. Bertocco, D. Goz, L. Tornatore, A. Ragagnin, G. Maggio, F. Gasparo et al., INAF trieste astronomical observatory information technology framework, in Astronomical Data Analysis Software and Systems XXIX, edited by R. Pizzo, E. R. Deul, J. D. Mol, J. de Plaa, and H. Verkouter, Vol. 527 of Astronomical Society of the Pacific Conference Series (2020), p. 303, arXiv:1912.05340.
- [68] https://www.desi.lbl.gov/collaborating-institutions
- [69] https://www.legacysurvey.org/
- [70] B. Bahr-Kalus, D. Parkinson, and K. Lodha, Data for "model-independent measurement of the matter-radiation equality scale in desi 2024", 10.5281/zenodo.17018002 (2025).
- [71] M. Abdul-Karim, A. G. Adame, D. Aguado, J. Aguilar, S. Ahlen *et al.* (DESI Collaboration), Data Release 1 of the dark energy spectroscopic instrument, arXiv:2503.14745.